Draft version June 29, 2015
Preprint typeset using LaTeX style emulateapj v. 01/23/15

RADIAL TRENDS IN IMF-SENSITIVE ABSORPTION FEATURES IN TWO EARLY-TYPE GALAXIES: EVIDENCE FOR ABUNDANCE-DRIVEN GRADIENTS

Nicholas J. McConnell [1], Jessica R. Lu [1], and Andrew W. Mann [2]

Draft version June 29, 2015

ABSTRACT

We have observed two massive early-type galaxies with Keck/LRIS and measured radial gradients in the strengths of stellar absorption features from 4000-5500 Å and 8000-10,000 Å. We present spatially resolved measurements of the dwarf-sensitive spectral indices Na I (8190 Å) and Wing-Ford FeH (9915 Å), as well as indices for species of H, C_2, CN, Mg, Ca, TiO, and Fe. Our measurements show a metallicity gradient in both objects, and Mg/Fe consistent with uniform α-enhancement, matching widely observed trends for massive early-type galaxies. The Na I index and the CN_1 index at 4160 Å exhibit significantly steeper gradients, with a break at $r \sim 0.1\,r_{\rm eff}$ ($r \sim 300$ pc). Inside this radius Na I and CN_1 increase sharply toward the galaxy center, relative to other indices. We interpret this trend as a rapid central rise in [Na/Fe] and [N/Fe]. In contrast, the FeH index exhibits a marginal decrease toward the galaxy center, relative to Fe. Our investigation is among the first to track FeH as a function of radius, and to demonstrate discrepant behavior between Na I and FeH. We suggest that the shallow gradient in FeH and steep, broken Na I profile reflect unique abundance patterns rather than a gradient in the stellar initial mass function.

1. INTRODUCTION

Driven primarily by observations within our own Galaxy, the assumption of a universal stellar initial mass function (IMF) throughout space and time has been employed in numerous studies of galaxy evolution. The canonical IMFs have the form of a power-law at high masses with $\mathrm{d}N/\mathrm{d}m \propto m^{-\alpha}$ and $\alpha = 2.3$ above $m > 0.5\,M_\odot$ (Kroupa 2001) or $m > 1\,M_\odot$ (Chabrier 2003). These IMFs then flatten and turn-over with a decreasing number of stars at masses below 0.5-1 $M_\odot$. In an extra-galactic context, key observables are influenced by the universal-IMF assumption, such as the galaxy mass function, mass-metallicity relation, and the correlation between total star formation rate and galaxy mass (e.g., Noeske et al. 2007; Wuyts et al. 2011; Leauthaud et al. 2012; Smit et al. 2012; Behroozi et al. 2013; Zahid et al. 2014; Salmon et al. 2015). Spectral energy density (SED) fitting is the most prevalent method for determining the stellar masses of intermediate- and high-redshift galaxies, and requires an assumed form of the IMF (e.g., Conroy et al. 2009; Marchesini et al. 2009). Consequently, claims of IMF variations deserve intense scrutiny (Bastian et al. 2010; Krumholz 2014) since any systemic IMF variation has broad implications for the inferred properties of galaxies and galaxy evolution.

In the past five years numerous studies have asserted that early-type galaxies with the largest velocity dispersions (σ) reveal a bottom-heavy IMF in their old stellar populations: an overabundance of stars with $m < 1\,M_\odot$ relative to the canonical IMFs of Kroupa (2001) or Chabrier (2003). Methodologies used to assess the IMF in these galaxies have included (1) examinations of stellar absorption features dominated by either giant or dwarf stars (e.g., Cenarro et al. 2003; van Dokkum & Conroy 2010, 2012; Conroy & van Dokkum 2012b; Ferreras et al. 2013; La Barbera et al. 2013; Spiniello et al. 2014), (2) comparisons of mass-to-light ratios from stellar population synthesis (SPS) and stellar dynamics (e.g., Cappellari et al. 2012, 2013b; Dutton et al. 2013; McDermid et al. 2014), (3) and comparisons between SPS and gravitational lensing (e.g., Treu et al. 2010; Spiniello et al. 2012; Posacki et al. 2015). Results with the most divergent IMFs show that the inferred slope of the IMF above $0.1\,M_\odot$ steepens to $\alpha \sim 3$ for the most massive early-type galaxies (e.g., La Barbera et al. 2013). Other studies have found a deviation between the average IMF in early-type galaxy samples and the canonincal IMF, without verifying a differential trend between different early-type galaxies (e.g., Auger et al. 2010; Dutton et al. 2012; Smith et al. 2012; Smith & Lucey 2013a). Alternatively, a few investigations have identified massive early-type galaxies with an IMF similar to the Milky Way (e.g., Smith & Lucey 2013b; Smith et al. 2015), or with a uniform IMF slope at $m > 8\,M_\odot$ (Peacock et al. 2014). Thus, it is still debated whether the IMF varies, how much the functional form changes, and how these variations depend on galaxy properties.

A limitation of the majority of IMF investigations in early-type galaxies is the use of a single spatial aperture per galaxy. For instance, stacked spectra from the Sloan Digital Sky survey (SDSS) have a fixed radius on the sky, blending data from less than and greater than one galaxy effective radius, $r_{\rm eff}$, from different galaxies (e.g., Ferreras et al. 2013; La Barbera et al. 2013; Spiniello et al. 2014). In contrast, the absorption-line studies by van Dokkum & Conroy (2012) and Conroy & van Dokkum (2012b) focus on the innermost regions of nearby galaxies, with a long-slit aperture of $r_{\rm eff}/8$. For lensing studies, the Einstein radius matches

[1] Institute for Astronomy, University of Hawaii at Mānoa, Honolulu, HI; nmcc@ifa.hawaii.edu
[2] Department of Astronomy, University of Texas at Austin, Austin, TX

a different physical radius in each galaxy, typically between $\sim 0.3\,r_{\rm eff}$ and $\sim 1\,r_{\rm eff}$ (e.g. Koopmans et al. 2009; Smith et al. 2015). Cappellari et al. (2012, 2013b) and McDermid et al. (2014) use resolved two-dimensional stellar kinematics, extending to 1 $r_{\rm eff}$ for many of the galaxies in their ATLAS$^{\rm 3D}$ sample. However, the most massive galaxies in ATLAS$^{\rm 3D}$ are not covered out to 1 $r_{\rm eff}$. At best, studies with different spatial footprints offer leverage for interpreting the role of IMF gradients within individual galaxies, although there are numerous complications from synthesizing heterogeneous and sometimes contradictory results. At worst, these studies all fail to distinguish between an IMF that varies only from galaxy to galaxy and IMF gradients within single galaxies.

Theoretical motivation for the presence of IMF gradients within early-type galaxies comes from models of inside-out growth, wherein massive galaxies are built first as compact starbursts and then accrete numerous smaller systems at large radii (e.g., Naab et al. 2009, 2014; Hopkins et al. 2010; Oser et al. 2012; Shankar et al. 2013). This model coincides with observations of size growth in massive red galaxies from redshifts $\sim$ 2 to the present (e.g., Trujillo et al. 2006; van Dokkum et al. 2010; Patel et al. 2013; van der Wel et al. 2014; Vulcani et al. 2014), and with the metal-poor stellar halos of nearby early-type galaxies (e.g., Coccato et al. 2010; Pastorello et al. 2014; Greene et al. 2012, 2015). If the IMF differs between low- and high-σ galaxies, then the most massive (and highest σ) early-type galaxies should naturally exhibit IMF gradients, as their outer regions have been assembled from smaller systems.

A second challenge for IMF investigations in early-type galaxies is the competing influence of elemental abundance ratios, which can drastically reshape stellar absorption features and subtly alter the mass-to-light ratio of stars. Some SPS models can vary the abundances of individual elements (e.g., Graves & Schiavon 2008; Conroy & van Dokkum 2012a). Yet the impacts of these abundance variations are woefully entangled with one another, and with the effects of IMF variations and other systematics such as isochrone offsets in temperature-luminosity space (Graves & Schiavon 2008; Conroy & van Dokkum 2012a; Spiniello et al. 2015). These same models have identified stellar absorption features that are especially sensitive to IMF variations, and targeted analyses of those features in observed galaxy spectra claim sufficient leverage to detect IMF variations robustly (e.g., Conroy & van Dokkum 2012b; La Barbera et al. 2013; Spiniello et al. 2014). However, abundance ratios are known to vary within individual galaxies (e.g., Strom et al. 1976; Tamura et al. 2000; Weijmans et al. 2009; Kuntschner et al. 2010; Greene et al. 2012, 2013, 2015), and the few investigations of IMF gradients in individual systems have offered scant analysis of single-element abundance variations (Martín-Navarro et al. 2015a,b,c).

Herein we examine two early-type galaxies, NGC 1023 and NGC 2974, for IMF and abundance gradients. For each object, we use long-slit spectra to probe spatial scales from $\sim$ 100 pc to a few kpc ($0.03\,r_{\rm eff}$ to $\sim 1\,r_{\rm eff}$). We present gradients in a selected set of stellar absorption line indices and qualitatively interpret their connection to stellar population gradients. We have paid special attention to the sodium doublet at 8190 Å (hereafter Na I) and the Wing-Ford iron hydride feature at 9915 Å (hereafter FeH), both of which are sensitive to the number density of cool dwarf stars. Our spectra also cover the giant-sensitive calcium triplet at 8500-8660 Å (hereafter Ca II), temperature-sensitive TiO features, numerous features of individual atomic species, and several Balmer lines.

Recently, Martín-Navarro et al. (2015a,b) analyzed long-slit spectra of four nearby early-type galaxies and reported IMF gradients in two ellipticals with large central σ (270-300 $\rm km\,s^{-1}$) and a mild gradient in the compact, high-σ galaxy NGC 1277. They inferred a uniform IMF slope in an elliptical galaxy with $\sigma \approx 100\,\rm km\,s^{-1}$. The two objects presented herein have central $\sigma \approx$ 210-250 $\rm km\,s^{-1}$, and our set of IMF-sensitive spectral indices has little overlap with those analyzed by Martín-Navarro et al. (2015a,b). Although our spectral coverage excludes the $\rm TiO_1$ and $\rm TiO_2$ features at 5960 Å and 6230 Å, we perform much more rigorous analysis of Na I and are among the first to present spatially resolved measurements of FeH.

We summarize the basic properties of NGC 1023 and NGC 2974 in Table 1. NGC 1023 is an SB0 galaxy, and NGC 2974 is an E4, as classified by the NASA/IPAC Extragalactic Database. Both galaxies are fast rotators (Emsellem et al. 2011). We selected both objects from the sample of van Dokkum & Conroy (2012), who observed the central $r_{\rm eff}/8$ of 34 early-type galaxies with identical spectral coverage to our investigation. Based on full-spectrum fitting to stellar population models, Conroy & van Dokkum (2012b) measured a stellar mass-to-light ratio, Υ_K, of $1.53\Upsilon_{K,\rm MW}$ in NGC 1023, and $1.45\Upsilon_{K,\rm MW}$ in NGC 2974, where $\Upsilon_{K,\rm MW}$ is the stellar mass-to-light ratio of the Milky Way disk. They infer that the central IMF in both galaxies is consistent with a Salpeter (1955) power-law ($\alpha = 2.35$) extending down to $0.1\,M_\odot$ and significantly more bottom-heavy than the Kroupa or Chabrier forms.

This paper is organized as follows. We summarize our long-slit observations in §2 and our data reduction methods in §3. In §4 we describe how absorption line indices are determined from our spectra, including random and systematic errors. We present radial trends for 13 selected line indices in §5. In §6 we offer a qualitative interpretation of the underlying stellar population trends in NGC 1023 and NGC 2974, with rigorous stellar population modeling deferred for future work. Our conclusions are briefly summarized in §7. Our two appendices contain detailed examinations of systematic errors in line index measurements, with particular focus on the Na I feature.

2. OBSERVATIONS

We observed NGC 1023 and NGC 2974 in December 2013 using LRIS on the Keck 1 telescope (Oke et al. 1995; Rockosi et al. 2010), in long-slit mode. LRIS comprises a red arm and a blue arm. For the red side, we used the 600 line $\rm mm^{-1}$ grating spanning 7500-10,800 Å, and on the blue side we used the 600 line $\rm mm^{-1}$ grism spanning 3100-5560 Å. Our slit was 0.7″ wide and spanned a length of 175″. The LRIS field of view is sampled by two detectors on each spectrograph arm, resulting in a

Table 1
Targets and Observations

Galaxy	D (Mpc)	M_K	$r_{\rm eff}$ ($''$)	σ_c ($\rm km\,s^{-1}$)	$[\rm Fe/H]_c$ dex	$[\rm Mg/Fe]_c$ dex	$[\rm Z/H]_c$ dex	$[\alpha/\rm Fe]_c$ dex	$\rm Age_c$ Gyr	Integration time (s)	Slit PA ($^\circ$)
(1)	(2)	(3)	(4)	(5)	(6)	(7)	(8)	(9)	(10)	(11)	(12)
NGC 1023	11.1	-24.01	47.8	217	-0.01	+0.18	+0.09	+0.19	11.7	13×600	85
NGC 2974	20.9	-23.62	38.0	247	-0.06	+0.20	+0.11	+0.29	8.9	14×600	45

Notes: We adopt distances, K-band absolute magnitudes, and effective radii (columns 2-4) from the ATLAS$^{\rm 3D}$ survey (Cappellari et al. 2011). Central velocity dispersions, [Fe/H], and [Mg/Fe] (columns 5-7) are adopted from Conroy & van Dokkum (2012b) and approximate an aperture size of $r_{\rm eff}/8$. Central [Z/H], [α/Fe], and stellar ages (columns 8-10) are adopted from Kuntschner et al. (2010), over an aperture of $r_{\rm eff}/8$.

coverage gap near the center of the slit. For the data presented herein, the gap spans $35''$ on the red side and $14''$ on the blue side. For this instrumental setup we measured a spectral resolution of ≈ 3.0 Å full width at half-maximum (FWHM) for both the blue arm and the red arm.

We placed our slit along the major axis of each galaxy with the galaxy center slightly offset from the chip gap. For a single exposure our spatial coverage extended from $\approx 60''$ on one side of the galaxy to $\approx 115''$ on the opposite side. Images were dithered between two positions that straddled the gap to achieve symmetric coverage of each galaxy. Additionally, a sky field $4'$ away was observed after every two to four science exposures. Total integration times for each target are included in Table 1. We completed more than two hours of integration time on each galaxy in order to obtain signal-to-noise ratios (S/N) ~ 100 per pixel in spatial bins near $1\,r_{\rm eff}$. The final spectra for NGC 1023 meet this criterion out to $1.6\,r_{\rm eff}$, for all features except the faint FeH band near 1 μm. For NGC 2974 the outermost bin with sufficient S/N spans 0.5-0.8 $r_{\rm eff}$.

Although our instrument setup matched that of van Dokkum & Conroy (2012), our observing pattern was selected to maximize spatial coverage and measure gradients in absorption line depths. In contrast, observations by van Dokkum & Conroy (2012) aligned the slit along the minor axis of each galaxy and used the far edges for in-frame sky subtraction. As a result, their previous analysis was restricted to the central few arc seconds of each galaxy, corresponding to an aperture of $r_{\rm eff}/8$.

3. DATA PROCESSING AND ANALYSIS

Our data reduction procedures largely follow the template described in van Dokkum & Conroy (2012). The notable exception is sky subtraction. Whereas van Dokkum & Conroy (2012) aligned the slit with the minor axis of each galaxy and used the far edges of the slit for sky subtraction, we wish to extract spectral features over the entire slit. To this end we recorded separate, non-concurrent sky exposures. On the red side, our sky subtraction requires careful wavelength calibration for each science frame, and a scaled subtraction procedure that adjusts the relative strengths of telluric emission line families, which vary on timescales of a few minutes. Details of these various calibration steps are described below, and representative cleaned spectra are illustrated in Figures 1 and 2.

3.1. *Instrumental Calibrations*

We use the `lpipe` software package[3] (Daniel Perley, private communication) for bias subtraction, flatfield correction, and cosmic ray cleaning. This package first determines and subtracts bias levels from the overscan region of each frame. Next it performs flatfielding using halogen lamp exposures taken at the end of the observing night, with the slit and disperser in place. The `lpipe` package coadds individual flatfield exposures, computes a boxcar-smoothed response spectrum for each row of the coadded flatfield, and divides each row by its matching response spectrum to produce a pixel-to-pixel flat. This flatfielding correction retains response variations along the spatial axis of the CCD, which are calibrated during the sky subtraction step (§3.2). After flat-fielding we split the raw frames into the separate CCD chips for each arm and process each chip independently.

On the red side, we use telluric OH emission lines to define a wavelength solution for each frame, using the IRAF routines `identify`, `fitcoords`, and `transform`. We divide each frame into blocks of 40 rows ($5.4''$) and extract a one-dimensional spectrum for each block. We fit a fifth-order polynomial to the peaks of the OH lines, converting pixels to Å. To calibrate for wavelength variation across each chip, we then fit a two-dimensional polynomial solution to the set of peak locations from all blocks. The 40-row extraction window permits reliable sky line fitting except for one or two blocks near the center of each galaxy; these blocks are masked from the two-dimensional fit.

The blue side includes a faint telluric line from NI at 5199 Å but is otherwise devoid of telluric emission features. We therefore derive a two-dimensional wavelength solution from daytime arc lamp frames, and assume that temporal variation in the wavelength solution can be described by a constant offset term at all wavelengths, along the entire slit. In some frames, the NI line is too faint to perform a useful fit. We therefore use the Fe5270 absorption feature at the galaxy center to measure the relative wavelength offsets across a sequence of frames. We anchor the frame-to-frame offsets to a single exposure for each galaxy, where the NI 5199 feature is strong enough to establish the absolute wavelength scale. In order to avoid substantial velocity structure when measuring the wavelength shifts in Fe5270, we only extract a $1.5''$ region

[3] The `lpipe` IDL routines are available at http://www.astro.caltech.edu/∼dperley/programs/lpipe.html.

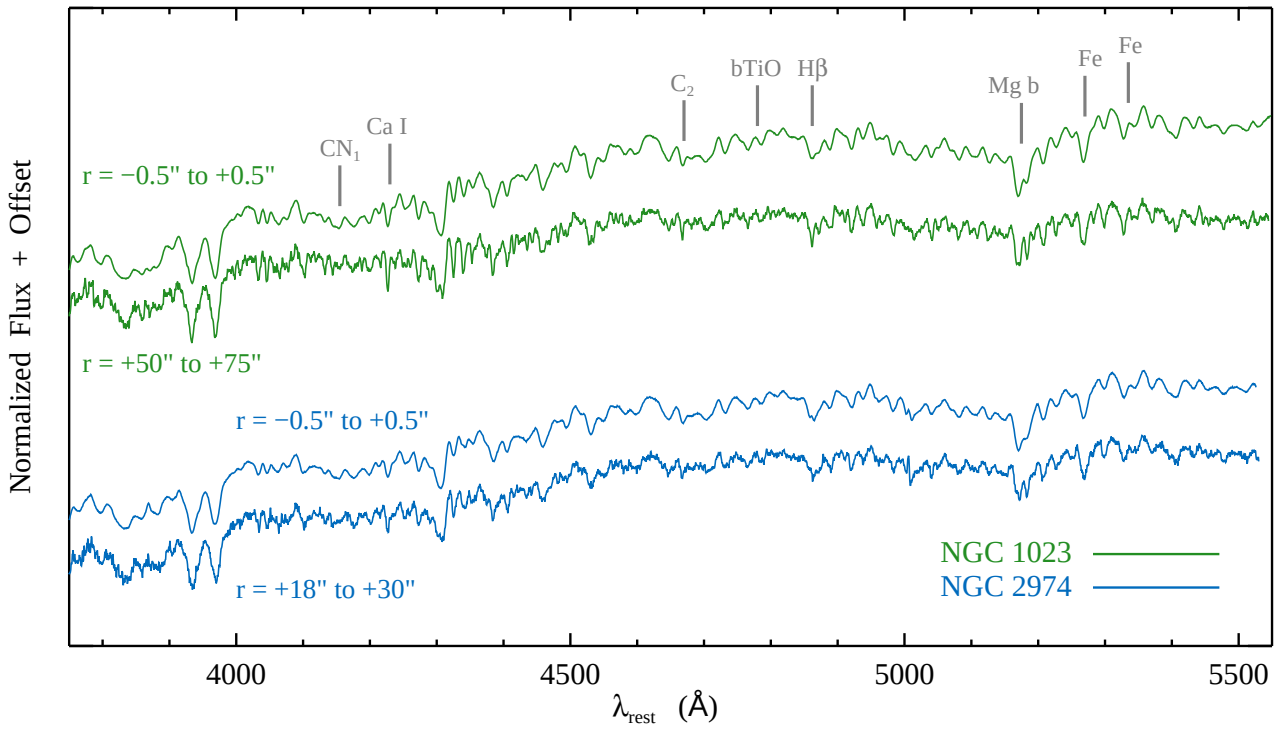

Figure 1. LRIS blue arm spectra extracted from the central and outer regions of NGC 1023 (top, green) and NGC 2974 (bottom, blue), and shifted to rest-frame wavelengths. Each spectrum has been sky-subtracted and flux-calibrated. Emission lines have been cleaned from the spectrum of NGC 2974. The spectra are normalized to the same median value, and constant offsets have been added for clarity. Stellar absorption features analyzed herein are labeled.

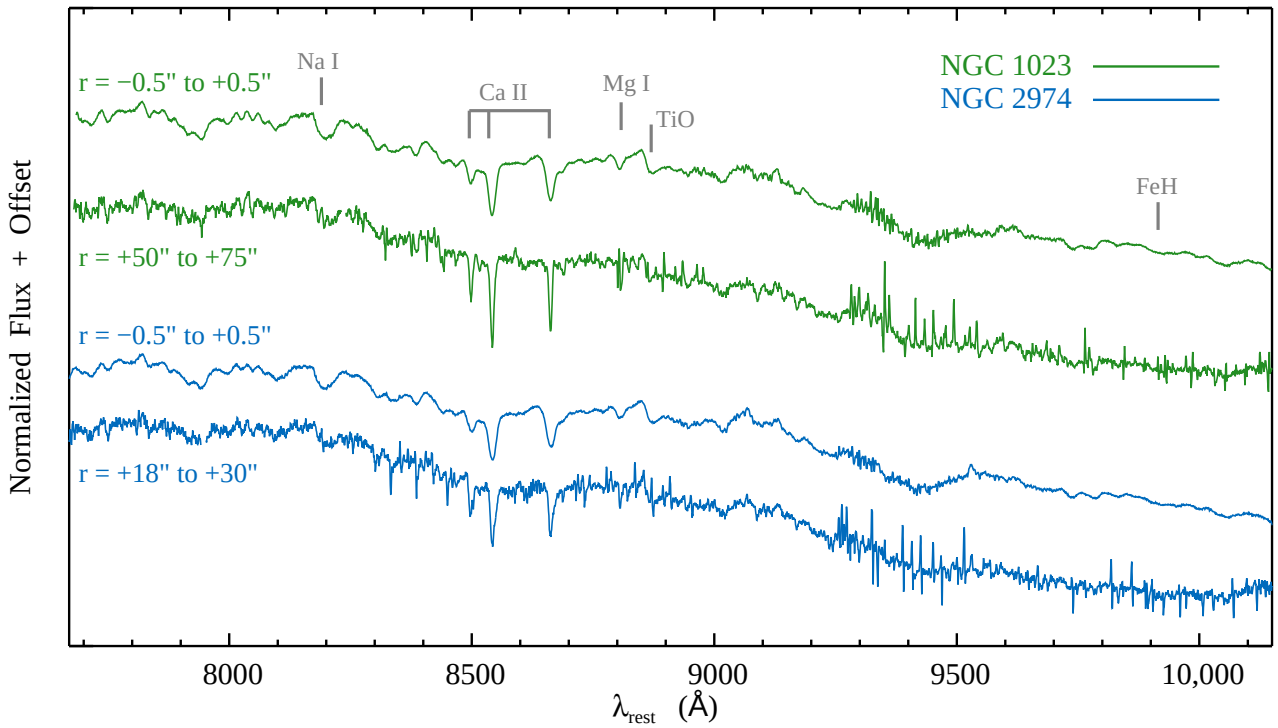

Figure 2. LRIS red arm spectra extracted from the central and outer regions of NGC 1023 (top, green) and NGC 2974 (bottom, blue), and shifted to rest-frame wavelengths. Each spectrum has been background-subtracted with a scaled sky spectrum, corrected for telluric absorption, and flux-calibrated. The spectra are normalized to the same median value, and constant offsets have been added for clarity. Stellar absorption features analyzed herein are labeled. The increased noise at 9200-9700 Å corresponds to strong telluric absorption bands.

at the galaxy center. We account for each galaxy's rotation curve once we have extracted final one-dimensional spectra for all spatial bins, and before we measure line indices (see §4).

3.2. *Sky Subtraction and Telluric Correction*

The background spectrum at red wavelengths is dominated by telluric emission lines, whose relative strengths vary on timescales comparable to our exposure times. Our goal of extracting galaxy light over the full length of the LRIS slit prohibits in-frame sky subtraction, and our sky frames must be corrected for variation in the line strengths. We extract a high-S/N sky spectrum from each science frame by applying a large aperture, offset from the galaxy center by at least 30″. We collapse the entire sky frame into a one-dimensional spectrum and use the `Skycorr` routine (Noll et al. 2014) [4] to perform scaled sky subtraction on the spectrum extracted from our science frame. `Skycorr` adjusts the relative amplitudes of OH and O_2 emission groups in the input sky spectrum to best match the input science-frame spectrum, and subtracts the rescaled sky spectrum to output a clean science spectrum.

Subtracting the `Skycorr` output spectrum from the initial science-frame spectrum yields a one-dimensional "master" sky spectrum for that particular frame. Next we use the halogen flats to compute the average response function of the CCD chip in the spatial dimension. We expand the master sky spectrum as a two-dimensional array, scaled by the spatial response function, and subtract this array from the science frame. Figure 3 illustrates the improvement in sky subtraction after performing this scaled sky procedure, relative to direct sky subtraction.

Residuals from telluric emission lines are our dominant source of noise near the FeH, MgI0.88, and TiO0.89 features (see Table 2 for definitions). These residuals are likely a combination of high shot noise from the bright lines, and wavelength calibration errors with magnitude < 0.1 Å. We have experimented with multiple variants of our sky subtraction procedure, including zoomed-in wavelength calibration over a narrow wavelength interval near the FeH band, fitting the wavelength solution with different polynomial orders, and applying `Skycorr` over narrower chunks of wavelength space. None of these attempts yielded clear improvements.

In addition to their native pixels, residuals from bright sky lines may contaminate adjacent pixels during smoothing, which we employ to bring spectra to a common σ (§4). To mitigate this, we perform a version of the iterative masking procedure described by van Dokkum & Conroy (2012). We first construct a mean sky spectrum for our observing night and flag the pixels corresponding to the brightest sky lines. We then mask these pixels at the corresponding wavelengths in each galaxy spectrum, such that their values are interpolated from nearby good pixels before smoothing. As the smoothing introduces undesired correlations between good pixels and masked pixels, we return to the unsmoothed spectrum and replace only the masked pixels with the smoothed output. We then perform the smoothing again, and iterate the substituting and smoothing steps five times. Although pixels near the edges of our masked regions are still over-weighted in our final spectrum, the iterations serve to distribute the excess weights more broadly.

[4] `Skycorr` and `SkyCalc` are available from the European Southern Observatory at http://www.eso.org/sci/software/pipelines/skytools

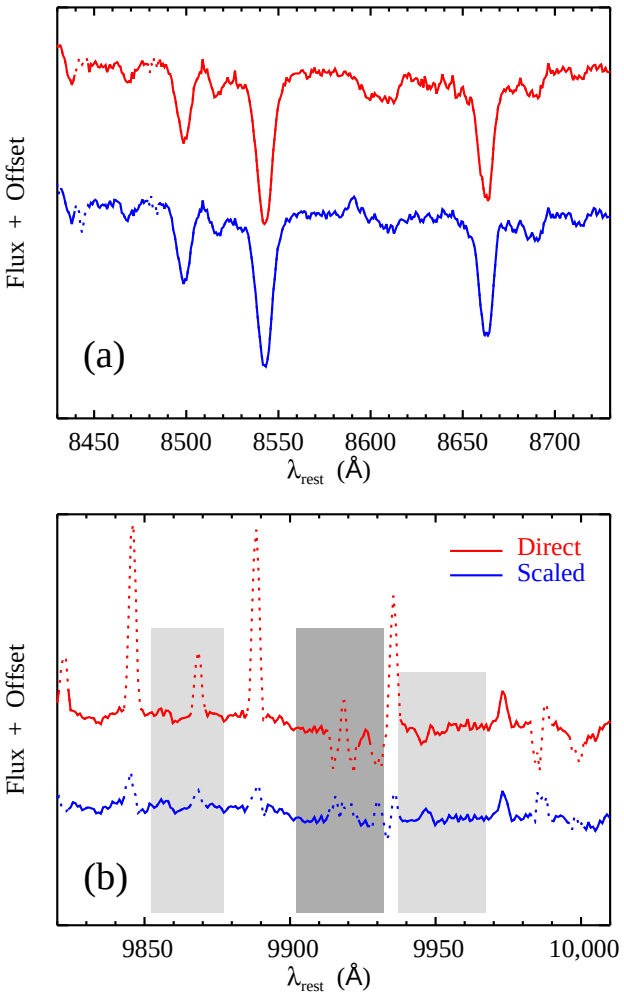

Figure 3. Sky-subtracted spectra extracted from +30″ to +50″ with respect to the center of NGC 1023. *Top:* region near the Ca II feature. *Bottom:* region near the FeH feature, with dark and light shaded areas corresponding to the line center and pseudo-continuum regions. In both panels, the red (upper) spectrum was obtained by directly subtracting sky frames from science frames, whereas the blue (lower) spectrum is our final spectrum after scaled sky subtraction. Even after scaled sky subtraction, pixels corresponding to bright sky lines exhibit excess noise. The dashed regions in each spectrum indicate areas that we masked before computing line indices.

In Figure 3b it is evident that the sky masking removes a substantial fraction of the FeH line region at 9902-9932 Å. In Appendix B we examine additional variants of the FeH index that extend the line region to 9962 Å. These variants contain a larger fraction of unmasked pixels and yield similar radial trends in the FeH index for $r < 0.5\,r_{\rm eff}$. As a second test, we have smoothed our spectra and measured line indices without any masking. The resulting index values do not differ significantly from the measurements we present below. Only the masked data exhibit a marginal upturn in MgI0.88 at large radii in NGC 1023 (Figure 5j). Otherwise, the radial trends

in MgI0.88 and FeH are qualitatively similar for masked and unmasked measurements.

After subtracting the sky emission spectrum, we correct each red arm frame for telluric absorption. We start with three transmission spectra from the `SkyCalc` sky model (Noll et al. 2012; Jones et al. 2013) [4] a baseline spectrum (T_B) for low airmass and low water vapor, a high-airmass spectrum (T_A), and a high water-vapor spectrum (T_W). After convolving each model spectrum to the instrumental resolution of the LRIS red arm, we form a grid of linear combinations (T_C):

$$T_C = T_B + \eta(T_A - T_B) + \omega(T_W - T_B) + \zeta \ . \quad (1)$$

For each exposure, we extract a spectrum from the central region of the galaxy, flatten it over the range 9250-9650 Å by dividing out a fourth-order polynomial, and determine the values of (η, ω, ζ) that best reproduce the observed telluric absorption over the wavelength range 9310-9370 Å. We then divide the frames on both CCD chips by the corresponding model T_C. At small radii, noise from our transmission correction dominates the galaxy spectra over the range $\sim$ 9200-9700 Å, where there are no stellar absorption features of interest. More importantly, a band of telluric H_2O overlaps the redshifted Na I feature in both galaxies, with a particularly strong transmission dip at 8230 Å observed wavelength. In Appendix A.3 we assess a plausible error range for the transmission spectra used to correct the Na I feature, and the corresponding error $\epsilon_{\rm tel}$ in our measurements of the Na I line index. We find that variations of 10% in our adopted transmission spectrum lead to errors of 15% and 6% in the Na I index for NGC 1023 and NGC 2974, respectively. These errors are incorporated along with other systematic terms in the line index measurements presented below (e.g., in Figures 5 and 6). We note that our empirically derived errors are much larger than the estimate of 0.1-0.2% by van Dokkum & Conroy (2012).

For our wavelength coverage on the blue side, the sky background is dominated by a continuum spectrum, and the background level was very stable during our observing night in December 2013. For the corresponding blue-arm data we directly subtract a calibrated sky frame from each calibrated science frame. Telluric absorption is negligible on the blue side.

3.3. *Position Registration*

For each science exposure, we trace the position of the galaxy center by fitting a two-component Gaussian profile to the central $\approx 5''$ of each galaxy, in each of 10 wavelength blocks. The resulting trace is interpolated to all wavelengths, and one-dimensional spectra are extracted with sub-pixel spatial precision at each wavelength, approximating the flux in each pixel to be evenly distributed in the spatial dimension. Each science exposure also includes one chip per arm that is offset from the galaxy center. We measure the spatial gap between the on-center and off-center chip by comparing the RA and DEC header keywords for alternating dither positions to the location of the galaxy center on the corresponding chips. For NGC 1023 and NGC 2974 the gap spans $35''$ on the red arm and $14''$ on the blue arm. This includes a small buffer region where the data frames are trimmed during initial calibration steps. To calibrate for wavelength-dependence of the trace on each off-center frame, we apply the trace from an adjacent exposure where the galaxy center is positioned on the corresponding chip.

3.4. *Spectral Response Calibration*

On the red side, we follow the flux calibration procedure of van Dokkum & Conroy (2012), which uses halogen flats to measure variations over small wavelength scales and calibrates large-scale variation with a white dwarf spectrum. We extract a one-dimensional halogen spectrum for each chip, apply 10-pixel boxcar smoothing, and divide the result into the extracted spectrum of a white dwarf calibration star. After this initial correction step, the white dwarf spectrum should approximate a λ^{-4} power law, with deviations on $\sim$ 100 Å scales arising from the intrinsic shape of the halogen spectrum. We divide the corrected white dwarf spectrum by a λ^{-4} function and fit the residual spectrum with a 10-point cubic spline. We then multiply the smoothed halogen spectrum for each chip by this smoothed residual profile, flattening the intrinsic source and yielding our final response curve.

On the blue side, the steep intrinsic spectrum of the halogen light source renders even preliminary calibration ineffective, and so we divide the observed white dwarf spectrum on each chip directly by λ^{-4}. To remove stellar features and pixel-to-pixel noise, we mask the pixels corresponding to Balmer absorption features, interpolate from the remaining wavelengths with a cubic spline, and perform 100-pixel boxcar smoothing to obtain a final response curve. Visual inspection of our blue-side halogen spectra reassures us that there is little response variation on scales < 50 Å.

4. MEASURING LINE INDICES

While some investigations of stellar populations employ full spectral fitting (e.g., Cid Fernandes et al. 2005; Koleva et al. 2009; Kuntschner et al. 2010; Conroy & van Dokkum 2012b; Podorvanyuk et al. 2013; Conroy et al. 2014; McDermid et al. 2015; Posacki et al. 2015; Wilkinson et al. 2015), line indices or equivalent widths of specific absorption features are useful for qualitative interpretation and can be readily applied to a number of SPS models (e.g., Trager et al. 2000a,b; Thomas et al. 2005; Schiavon 2007; Graves & Schiavon 2008; La Barbera et al. 2013; Spiniello et al. 2014). In Table 2 we list the definitions of 13 line indices discussed herein. On the blue side we track prominent indices from the Lick/IDS system, introduced by Faber et al. (1985) and updated by Worthey et al. (1994) and Trager et al. (1998), as well as the bTiO index from Spiniello et al. (2014). Our wavelength coverage with the LRIS blue arm cuts off in the middle of their aTiO feature. At near-infrared wavelengths, we adopt line index definitions for Na I, Ca II, FeH, TiO, and Mg from Conroy & van Dokkum (2012a, hereafter CvD12).

La Barbera et al. (2013) introduced an alternative definition for the Na I index, whose pseudo-continuum regions traced smaller residuals between stellar population models and galaxy spectra from SDSS. We describe this feature, Na $I_{\rm SDSS}$, in Table 2. In Appendix B we examine the radial behavior of Na $I_{\rm SDSS}$ and three new variants

Table 2
Line Index Definitions

Index	Ref.	Line (Å)	Blue Pseudo (Å)	Red Pseudo (Å)	Units	Dependence
CN_1	1	4142.1 - 4177.1	4080.1 - 4117.6	4244.1 - 4284.1	mag	C↑, N↑, O↓, age↑
Ca4227 (CaI0.42)	1 (2)	4222.2 - 4234.8	4211.0 - 4219.8	4241.0 - 4251.0	Å	Ca↑, age↑, C
$C_2$4668 ($C_2$0.47)	1 (2)	4634.0 - 4720.2	4611.5 - 4630.2	4742.8 - 4756.5	Å	C↑, O↓, age↑
bTiO	3	4758.5 - 4800.0	4742.8 - 4756.5	4827.9 - 4847.9	mag	$T_{\rm eff}$ ↓, g ↑, Mg↑, O↑, Ti↑, C↓
Hβ	1	4847.9 - 4876.6	4827.9 - 4847.9	4876.6 - 4891.6	Å	age↓
Mg b (MgI0.52a)	1 (2)	5160.1 - 5192.6	5142.6 - 5161.4	5191.4 - 5206.4	Å	Mg↑, age↑, $T_{\rm eff}$ ↓
Fe5270 (FeI0.52)	1 (2)	5245.6 - 5285.6	5233.2 - 5248.2	5285.6 - 5318.2	Å	Fe↑, age↑
Fe5335 (FeI0.53)	1 (2)	5312.1 - 5352.1	5304.6 - 5314.9	5353.4 - 5363.4	Å	Fe↑, age↑
Na I (NaI0.82)	2	8174.8 - 8202.7	8167.8 - 8174.8	8202.7 - 8212.7	Å	Na↑, g ↑, $T_{\rm eff}$ ↓, α ↓, age↑
$\rm Na\,I_{SDSS}$	4	8177.8 - 8197.7	8140.8 - 8150.8	8230.7 - 8241.7	Å	Na↑, g ↑, $T_{\rm eff}$ ↓, α ↓, age↑
Ca II=Ca1+Ca2 +Ca3						
Ca1	2,4,5	8481.7 - 8510.7	8471.7 - 8481.7	8560.6 - 8574.6	Å	Ca↑, g ↓, Na↓, $T_{\rm eff}$ ↑
Ca2	2,4,5	8519.7 - 8559.6	8471.7 - 8481.7	8560.6 - 8574.6	Å	Ca↑, g ↓, Na↓, $T_{\rm eff}$ ↑
Ca3	2,4,5	8639.6 - 8679.6	8616.6 - 8639.6	8697.6 - 8722.6	Å	Ca↑, g ↓, Na↓, $T_{\rm eff}$ ↑
MgI0.88	2	8799.5 - 8814.5	8775.0 - 8787.0	8845.0 - 8855.0	Å	Mg↑, age↑, $T_{\rm eff}$
TiO0.89	2		8832.6 - 8852.6	8867.6 - 8887.6	ratio	$T_{\rm eff}$ ↓, O↑, Ti↑, C↓
FeH (FeH0.99)	2	9902.3 - 9932.3	9852.3 - 9877.3	9937.3 - 9967.3	Å	Fe↑, $T_{\rm eff}$ ↓, g ↑

Notes: The index definitions above use air wavelengths, as do all figures in this paper. The TiO0.89 index is defined as the flux ratio for the blue pseudo-continuum divided by the red pseudo-continuum. The last column lists some of the main atomic species and stellar atmosphere properties that influence the depth of each feature. For integrated light, $T_{\rm eff}$ reflects the relative contribution of warm vs. cool stars, surface gravity g reflects the relative contribution of giants vs. dwarfs, and α reflects the combined abundances of α-process elements. Arrows indicate whether the absorption index increases or decreases with respect to an increase in the respective quantity. For instance, g ↑ means the index becomes stronger with increasing surface gravity; i.e. the feature is dwarf-sensitive. References: (1) Trager et al. 1998; (2) Conroy & van Dokkum 2012a; (3) Spiniello et al. 2014; (4) La Barbera et al. 2013; (5) Cenarro et al. 2001.

of the FeH index, to test for biases that might arise from overlapping absorption features or contamination by sky lines. In brief, we find that the choice of Na I or FeH definition does not change the essential radial trends we observe (§5), or our interpretation (§6).

Our spatial binning scheme for each galaxy is designed to maximize S/N in each aperture, while retaining the ability to compare data near $0.5\,r_{\rm eff}$ and $1.0\,r_{\rm eff}$. Between $\sim 0.2\,r_{\rm eff}$ and $\sim 1\,r_{\rm eff}$ our bin sizes range from $5''$ to $20''$. At smaller radii, increased surface brightness permits us to employ much finer binning, down to seeing-limited scales $\approx 1.0''$. In each two-dimensional science frame we determine an aperture according to the spatial registration described in §3.3, and at each wavelength we measure the mean flux over the corresponding rows. Our spatial mean includes 3-σ clipping at radii where the surface brightness profile is sufficiently shallow, typically $r > 5''$. Once spectra have been extracted from individual science frames, they are coadded via direct summation.

To assess spatial gradients in line indices, we must compare spectra with the same velocity dispersion σ, in a common rest frame. To this end, we measure σ and the radial velocity v for each spatially binned spectrum (§5), and apply a Gaussian smoothing kernel so as to artificially raise σ to a common value. The kernel width is chosen such that each binned spectrum has a final dispersion of $230\,{\rm km\,s^{-1}}$ for NGC 1023 and $245\,{\rm km\,s^{-1}}$ for NGC 2974, matching our highest measurement of σ in each galaxy. We also shift the wavelength grid for each spectrum to rest-frame wavelengths, based on our measurement of v. Figure 4 illustrates spectra near the Na I, Ca II, and FeH features, after performing kinematic calibrations. Our measurements of v and σ employ the `pPXF` procedure by Cappellari & Emsellem (2004). In Appendix A.1 we discuss possible systematic errors in measuring kinematics, and the resulting impact on our measurements of line indices.

The blue-arm spectra of NGC 2974 include strong emission lines, which must be removed before measuring the depths of nearby absorption features. We fit and subtract an emission line component for each blue-arm spectrum by including Gaussian emission line profiles for H, NI, OII, and OIII in our list of kinematic templates for `pPXF`. We explore uncertainties and alternative methods for the emission line fitting in Appendix A.2. NGC 1023 shows much subtler traces of emission, which we also discus in Appendix A.2.

Once our spectra are cleaned and calibrated for kinematics, we compute equivalent widths using the formulae of Worthey et al. (1994, Equations 1-3), whereby the continuum level is modeled as a straight line connecting the midpoints of the red and blue pseudo-continuum bands in Table 2. Our only exception is the TiO0.89 index, which is expressed as the ratio of blue to red pseudo-continuum levels as defined by CvD12.

4.1. *Random and Systematic Errors*

In principle, noise in a galaxy spectrum can be propagated analytically to compute formal statistical errors in an ensuing equivalent width measurement. Yet noise from sky subtraction and telluric absorption is not random and uncorrelated in our spectra. Instead of formal error propagation, we perform a simpler and more empirical estimate of line index measurement errors, as follows.

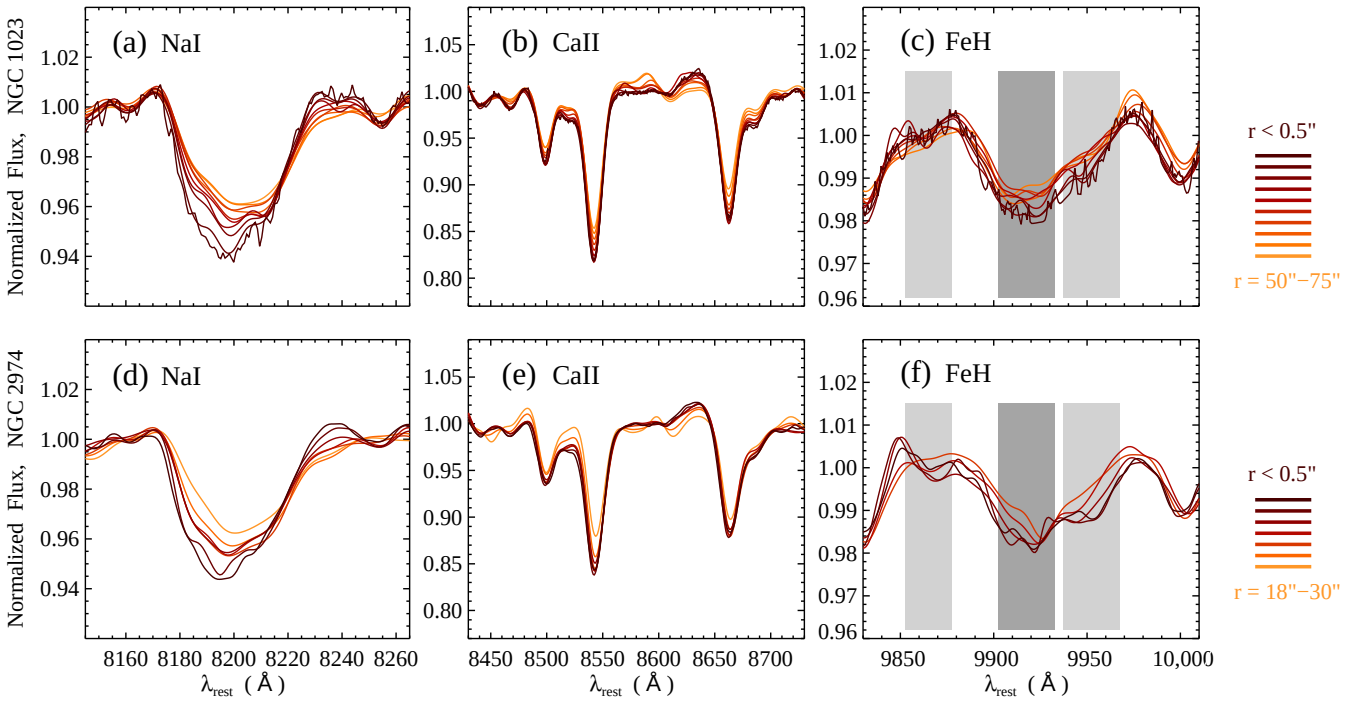

Figure 4. Comparison of spectra at multiple radial bins in each galaxy, featuring the gravity-sensitive absorption features Na I (left), Ca II (middle), and FeH (right). For visualization purposes only, we have divided each spectrum by a third-order polynomial. Each spectrum has been convolved to a velocity dispersion matching the central radial bin. Top row: NGC 1023, convolved to $\sigma = 230\,\mathrm{km\,s^{-1}}$. Bottom row: NGC 2974, convolved to $\sigma = 245\,\mathrm{km\,s^{-1}}$. For FeH, light and dark rectangles indicate the line and pseudo-continuum regions, respectively.

We split the science frames for each galaxy into two subsets, with frames from each dither position evenly distributed. We extract one-dimensional spectra from each frame, matching the spatial apertures in §5, and coadd all the spectra within a subset. After pairing data from opposite sides of the galaxy and measuring indices as described above, we have four index measurements for each interval in r. We adopt the mean and standard deviation of these measurements as our final equivalent width and 1σ random error. We then add the random errors in quadrature with the total systematic error $\epsilon_{\rm sys}$ from kinematic uncertainties, emission line removal, and telluric absorption. We derive $\epsilon_{\rm sys}$ in Appendix A and summarize its value for each index in Table 3.

For most of the line indices we have investigated, $\epsilon_{\rm sys}$ is comparable to the random deviations between our four subsets of data, particularly at radii $\lesssim 10''$ where our spectra have very high S/N. Exceptions where random variance dominates systematic errors at all radii are the bTiO index in NGC 1023, the Ca II index in NGC 2974, and the TiO0.89 and FeH indices in both galaxies. For the FeH feature in particular, the noise including sky lines exceeds the 3.5% total systematic error by at least a factor of two. Our error bars in Figures 5 and 6 below include both random and systematic terms.

The largest systematic effects occur for Na I and are discussed extensively in Appendix A. In particular, we note that the sizable error bars for Na I in NGC 1023 (Figure 5h) are largely driven by the 15% $\epsilon_{\rm tel}$ term for possible errors in telluric correction (Appendix A.3). While this term is important for considering the absolute strength of the Na I index, any bias introduced by telluric correction will be uniform with radius. Therefore, radial trends in Na I are more significant than suggested by Figure 5. In NGC 2974, $\epsilon_{\rm tel}$ is only 6% and is comparable to other terms in the total error budget. When $\epsilon_{\rm tel}$ is excluded, the remaining systematic error in Na I ranges from 7-12%.

Moreover, van Dokkum & Conroy (2012) have suggested that the scatter in the relation between Na I strength and the center of the Na I+TiO blend provides a heuristic upper limit for the total error in the measured Na I index. In essence, if the only varying quantity is the Na I component of the Na I+TiO blend, this will drive a tight anti-correlation between the blend center and the Na I index strength. Additional scatter in the relation reflects a combination of measurement errors in the Na I index and blend center, and independent variation of the TiO component. We have performed a linear fit to this relation for each galaxy, estimating the blend center as the wavelength of minimum flux between 8180 Å and 8230 Å. With respect to our best fit, we find a scatter in Na I of 0.08 Å for NGC 1023 and 0.06 Å for NGC 2974. These values are indeed comparable to our combined random and systematic errors in Na I, which range from 0.06-0.12 Å for NGC 1023 and 0.05-0.07 Å for NGC 2974. If anything, this test indicates that we have assessed our systematic errors conservatively.

5. RESULTS: SPATIAL VARIATION IN LINE DEPTHS

The radial variations in the Na I, Ca II, and FeH spectral features are illustrated in Figure 4, after convolving binned spectra to the same rest frame and velocity dispersion. In both galaxies, the Na I and Ca II fea-

tures become visibly shallower toward larger radius. At $\sigma \sim 200\,\mathrm{km\,s^{-1}}$, the Na I doublet (8183 and 8195 Å) is unresolved, and blended with a TiO band at 8205 Å. In the left panels of Figure 4 it is apparent that as the Na I blend becomes shallower toward large radii, its center shifts toward redder wavelengths, an indication that Na I is driving the change in depth rather than TiO.

From Figure 4 it is evident that the trend toward shallower FeH at large r is present in both the line region and the red pseudo-continuum region defined by CvD12. While the CvD12 definition highlights the deepest part of the FeH bandhead, their red pseudo-continuum still includes contributions from FeH and possibly TiO. To ensure that radial variations in the pseudo-continuum near FeH are not dominating our index measurements, we have tested three alternative variants of the FeH index, including two that extend the line region to 9962 Å. Details are provided in Appendix B. All variants yield similar trends in FeH with respect to r near the centers of NGC 1023 and NGC 2974.

Radial trends in measured line indices are shown in Figure 5 for NGC 1023 and Figure 6 for NGC 2974. We group the Hβ, bTiO, and TiO0.89 indices as indicators of age and temperature; the CN_1, C_24668, and $\langle$Fe$\rangle$ indices as indicators of C, N, or Fe abundance [5]; the Mg b, MgI0.88, and Ca4227 indices as indicators of α-process elements; and the Na I, Ca II, and FeH indices as IMF-sensitive indicators. Nonetheless, we stress that variations in the underlying stellar population have degenerate effects on multiple indices, and no single index or set of indices maps directly to a single stellar population property. In particular, we will inspect the meaning of Na I more carefully in §6.1.1.

All of the absorption features (except FeH in NGC 2974) weaken toward large radii, as expected for galaxies harboring metallicity gradients. Yet there are noteworthy differences between the rate of decline for different indices. The very shallow gradient in Hβ implies a nearly uniform stellar age, which is consistent with other observations (Kuntschner et al. 2010). In contrast, Na I and CN_1 exhibit steep gradients that appear nearly constant in $\log(r)$, while other features decline less steeply on average, and/or turn over toward a flat profile in the central kpc. Interestingly, the Wing-Ford FeH band does not mirror the steep radial increase exhibited by Na I, although both are dwarf-sensitive features. In both galaxies, our measurements of FeH are consistent with uniform strength out to $0.2\,r_{\rm eff}$. Beyond this radius, NGC 1023 shows a gradual decline in FeH strength. NGC 2974 shows subtle evidence for increasing FeH strength toward large radii, but our outermost points for this galaxy are badly contaminated by telluric emission. The Ca4227, Mg b, and $\langle$Fe$\rangle$ indices all exhibit similar radial behavior, with a decline of 15%-25% per dex in r. Our trends in Hβ, Mg b, and $\langle$Fe$\rangle$ are broadly similar to those measured by Kuntschner et al. (2006) with SAURON integral-field data out to $r \approx 20''$. Yet at large r we find lower Mg b values than Kuntschner et al. (2006) in both NGC 1023 and NGC 2974.

We display ratios of selected line indices in Figures 7-9. For these figures, we have switched to a linear scale in radius so as to emphasize rapid changes within the central region of each galaxy. We have also removed the telluric absorption term from our error bars in Na I, as justified in §4.1. In Figure 7 we compare the Na I index to six other species. In every case except for CN_1, the relative strength of Na I increases toward the galaxy center, with a particularly steep rise in the innermost $0.1\,r_{\rm eff}$. This region turns out to be very similar to the $r_{\rm eff}/8$ aperture size used by van Dokkum & Conroy (2012).

In Figures 8 and 9 we compare the radial variation of IMF-sensitive and α-element indices, relative to $\langle$Fe$\rangle$. Remarkably, the Na I and FeH indices show opposite trends with respect to $\langle$Fe$\rangle$ in the central $0.1\,r_{\rm eff}$, even though Na I and FeH are both touted as dwarf-sensitive features. As in Figure 7e, Na I/$\langle$Fe$\rangle$ rises dramatically in the central $0.1\,r_{\rm eff}$ of each galaxy. On the other hand, FeH/$\langle$Fe$\rangle$ decreases by $\sim$ 10-20%. Deviations from constant FeH/$\langle$Fe$\rangle$ ought to indicate changes in the fraction of cool dwarf stars. If this is the case, then the opposing variation in Na I is difficult to reconcile. Even considering the large uncertainties in our measurements, the deviation between Na I strength and FeH strength appears to be significant (Figure 7f).

The near constancy of Mg b/$\langle$Fe$\rangle$ and Ca4227/$\langle$Fe$\rangle$ at all radii preliminarily suggests the absence of a gradient in [α/Fe], whereas Ca II/$\langle$Fe$\rangle$ decreases from $r \sim 0.1\,r_{\rm eff}$ toward the galaxy center. This decline in Ca II relative to $\langle$Fe$\rangle$ and other Ca and Mg features could arise from a lower fraction of giant stars in the very center of the galaxy, or from an increase in sodium abundance (e.g., CvD12). Both effects predict a simultaneous increase in Na I strength. In §6.1.1 we argue that sodium abundance drives the radial variations in Na I and Ca II.

While the Na I gradients in NGC 1023 and NGC 2974 are largely consistent, the CN_1 index shows mild discrepancies between the two galaxies. The overall gradient in CN_1 is approximately -0.06 mag per dex in r for NGC 1023, versus -0.04 mag dex^{-1} for NGC 2974. This difference corresponds to a shallow decrease in Na I/CN_1 toward the center of NGC 1023, versus a shallow increase for NGC 2974 (Figure 7b).

6. DISCUSSION

Variations in stellar masses, ages, and abundance ratios impose degenerate effects upon individual line indices. Inferring these physical properties demands an intricate comparison between observed data and stellar population and stellar evolution models. Herein we have attempted to present our measurements with sufficient transparency to support future analyses employing a wide range of modeling assumptions. With the caveat that rigorous interpretation requires careful modeling, we shall discuss some qualitative trends in the relative strengths of different line indices as a function of radius, in light of previously established connections to physical stellar properties (§6.1). In §6.1.5 and §6.2 we compare our results to predicted trends from SPS models (CvD12), and to other recent investigations of radial IMF variations in early-type galaxies.

6.1. *Physical Interpretation of Line Index Gradients*

The gradual decline in all heavy-element indices toward large radii indicates the presence of an overall metallicity gradient, while Mg b/$\langle$Fe$\rangle$ is higher than solar abun-

[5] We define $\langle$Fe$\rangle \equiv 0.5$(Fe5270 + Fe5335), following Trager et al. (2000a).

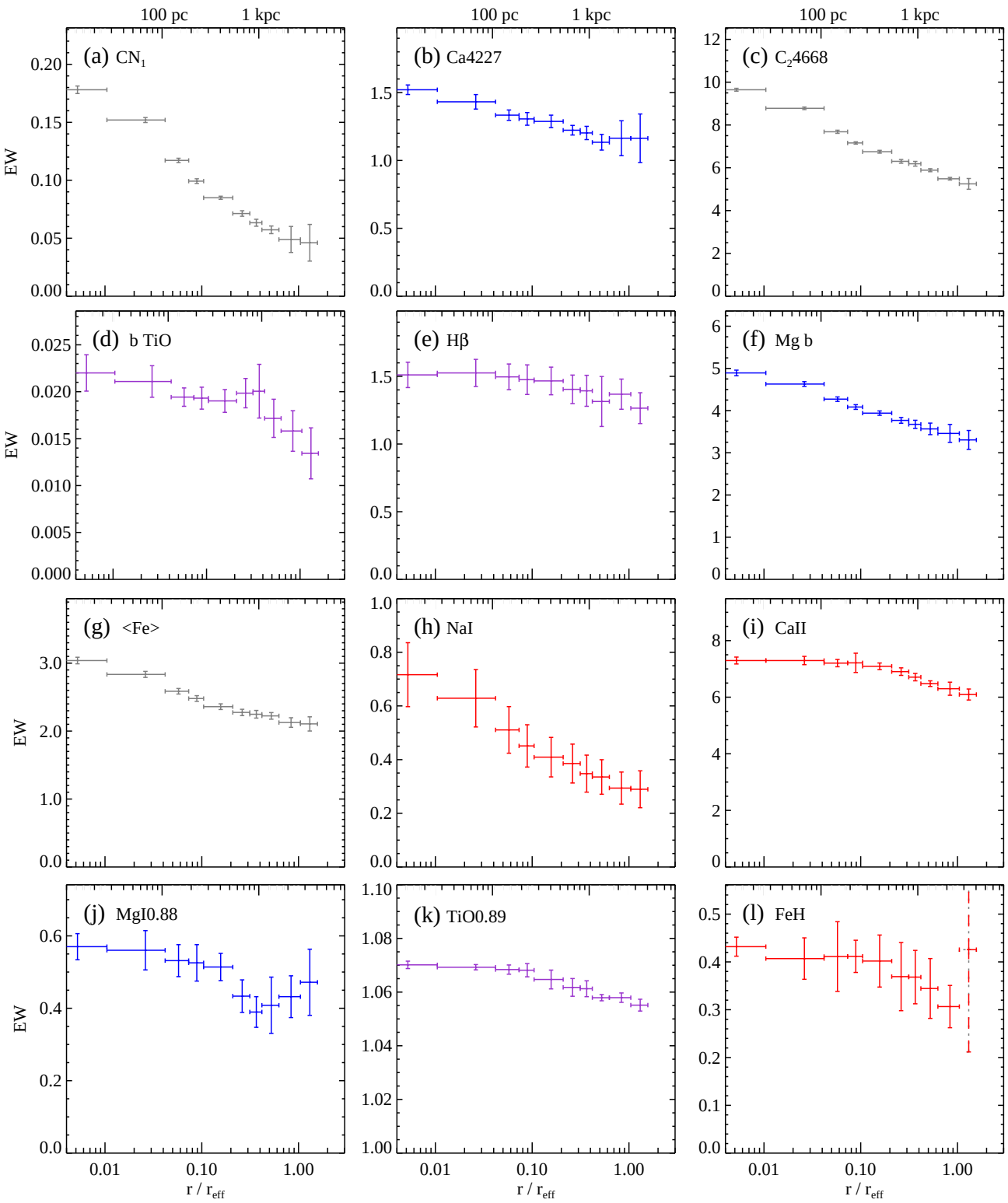

Figure 5. Selected line index strengths vs. radius in NGC 1023, corresponding to $\sigma = 230\,\mathrm{km\,s^{-1}}$. Vertical errors include systematic effects discussed in Appendix A, and horizontal error bars indicate the radial bin sizes. Panels are ordered by wavelength and color-coded according to each index's primary use as a diagnostic: grey (panels a, c, and g) for indicators of C, N, and Fe abundance; blue (panels b, f, and j) for α-element indicators; purple (panels d, e, and k) for stellar age and effective temperature indicators; and red (panels h, i, and l) for IMF indicators. However, we stress that simultaneous modeling of multiple indices is necessary to quantitatively assess the contributions of star formation history, IMF, and abundances of individual elements. Most panels have units of Å for equivalent width, except for CN_1 and bTiO (magnitudes), and TiO0.89 (ratio of blue to red pseudo-continuum). The y-axis in each panel scales from 0 to 1.3 times the maximum line depth. The last data point in panel l (FeH, dashed error bar) is severely compromised by sky emission. Tabulated index values are available as online data.

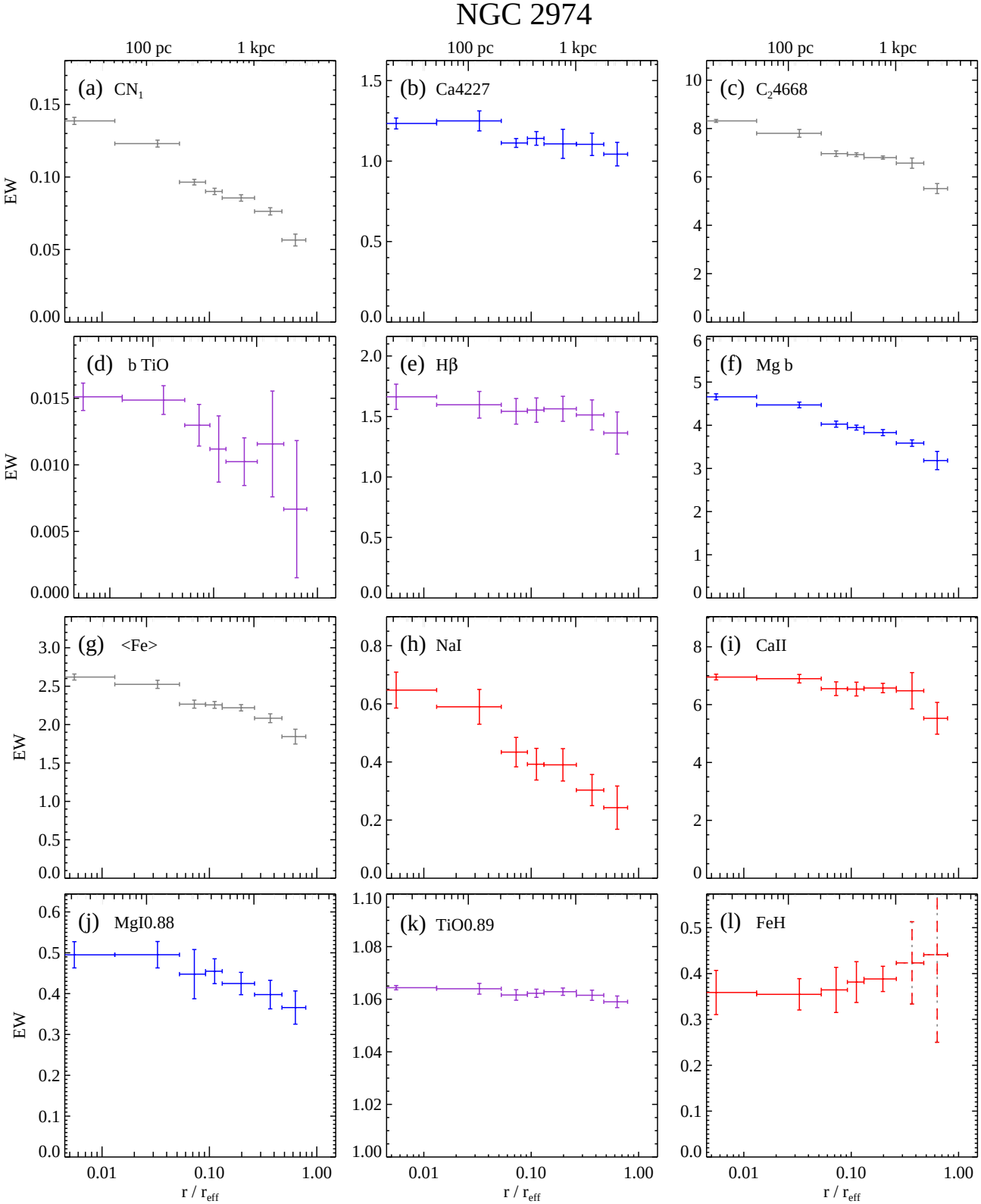

Figure 6. Selected line index strengths vs. radius in NGC 2974, corresponding to $\sigma = 245\,\mathrm{km\,s^{-1}}$. Color codings and equivalent width units are the same as in Figure 5. The y-axis in each panel scales from 0 to 1.3 times the maximum line depth. The last two data points in panel l (FeH, dashed error bar) are severely compromised by sky emission. Tabulated index values are available as online data.

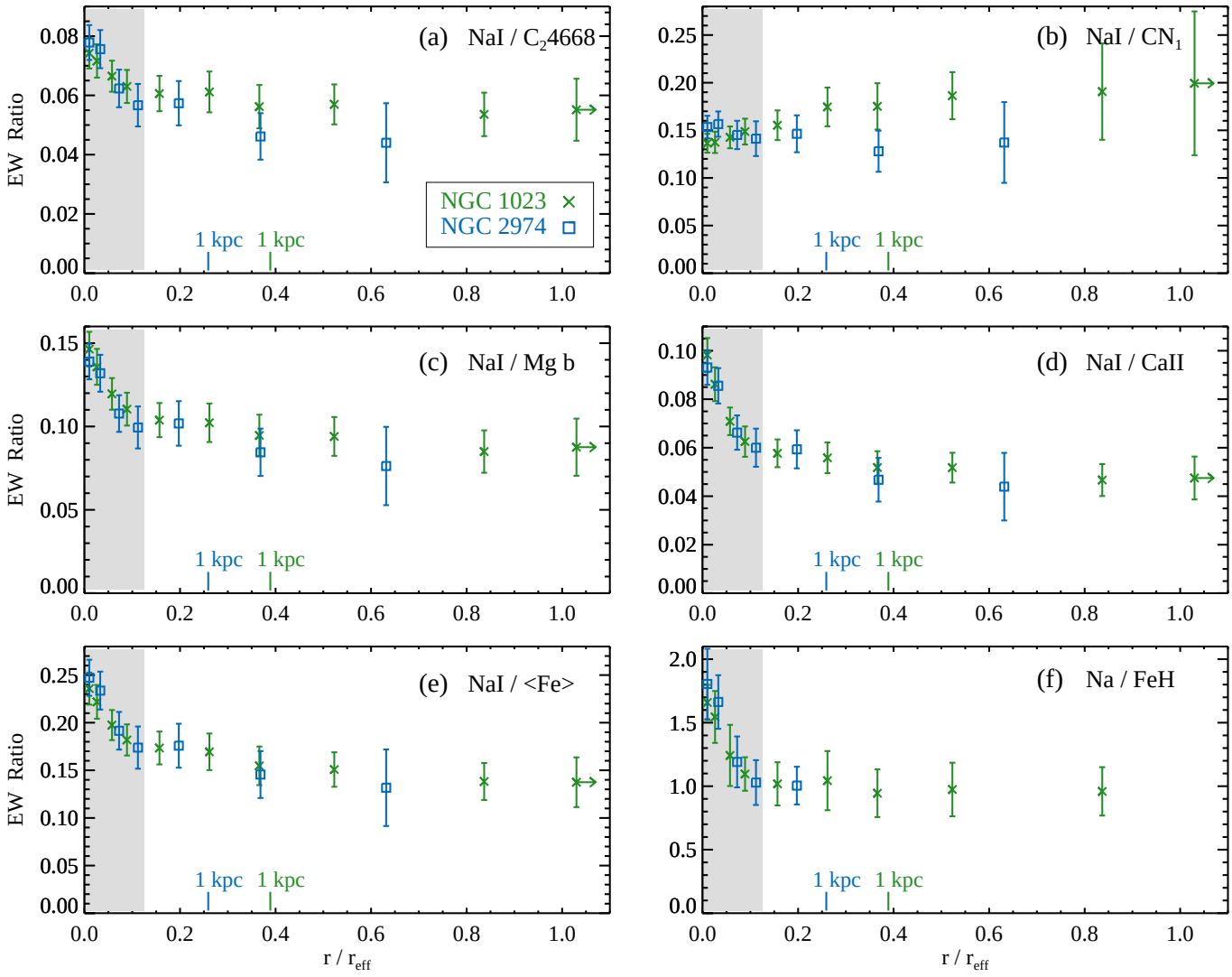

Figure 7. Ratio of Na I to other selected line indices as a function of radius in NGC 1023 (green) and NGC 2974 (blue). The spatial binning is the same as Figures 5-6, but plotted on a linear scale. In panels a-e, the outermost spatial bins extend to $1.6\,r_{\rm eff}$ for NGC 1023 and $0.8\,r_{\rm eff}$ for NGC 2974. For panel f (Na I/FeH), the outermost bins extend to $1.0\,r_{\rm eff}$ for NGC 1023 and $0.26\,r_{\rm eff}$ for NGC 2974. Grey shaded areas indicate the scale of the single-aperture measurements by van Dokkum & Conroy (2012), corresponding to a physical radius of 320 pc in NGC 1023 and 480 pc in NGC 2974. Error bars include systematics from measuring kinematics and removing emission lines, but do not include a component for telluric correction of Na I (see Appendix A.3). For panel b, we measured the CN_1 equivalent width in Å before comparing to Na I.

dances and is nearly constant out to $\sim 1\,r_{\rm eff}$. The Mg b and ⟨Fe⟩ indices are widely used to infer total metallicity [Z/H] and enhancement of α-process elements, [α/Fe]. Our results agree with observations of metallicity gradients and spatially uniform α-enhancement in large samples of early-type galaxies. Specifically in NGC 1023 and NGC 2974, Kuntschner et al. (2010) measured [α/Fe] $\approx +0.2$ dex out to $\approx 20''$ in both galaxies, as well as shallow but significant metallicity gradients: from $r_{\rm eff}/8$ to $r_{\rm eff}$, [Z/H] drops from +0.09 to -0.03 in NGC 1023 and from +0.11 to +0.01 in NGC 2974.

The aggregate abundance ratios [Z/H] and [α/Fe] depend heavily upon oxygen abundance, which is very difficult to infer directly from stellar absorption features (e.g., Schiavon 2007). In many circumstances the production of metals and α-process elements can be traced by the more empirical metrics [Fe/H] and [Mg/Fe]. Conroy & van Dokkum (2012b) have measured [Fe/H] and [Mg/Fe] for the central $r_{\rm eff}/8$ of NGC 1023 and NGC 2974, and their measurements are broadly consistent with those by Kuntschner et al. (2010). Both sets of central measurements are included in Table 1 above. Although the [Z/H] values from Kuntschner et al. (2010) are larger than the [Fe/H] values from Conroy & van Dokkum (2012b), they can be reconciled via the observed α-enhancement and the range of uncertainty in [O/Mg] (see, e.g., the conversion by Trager et al. 2000b and discussion by Greene et al. 2015).

Our measurements of shallow radial variation in Hβ are consistent with the two-dimensional SAURON maps and aperture-based fits by Kuntschner et al. (2010), which reveal no evidence for age gradients in NGC 1023 or NGC 2974. Assuming a uniform star formation history greatly

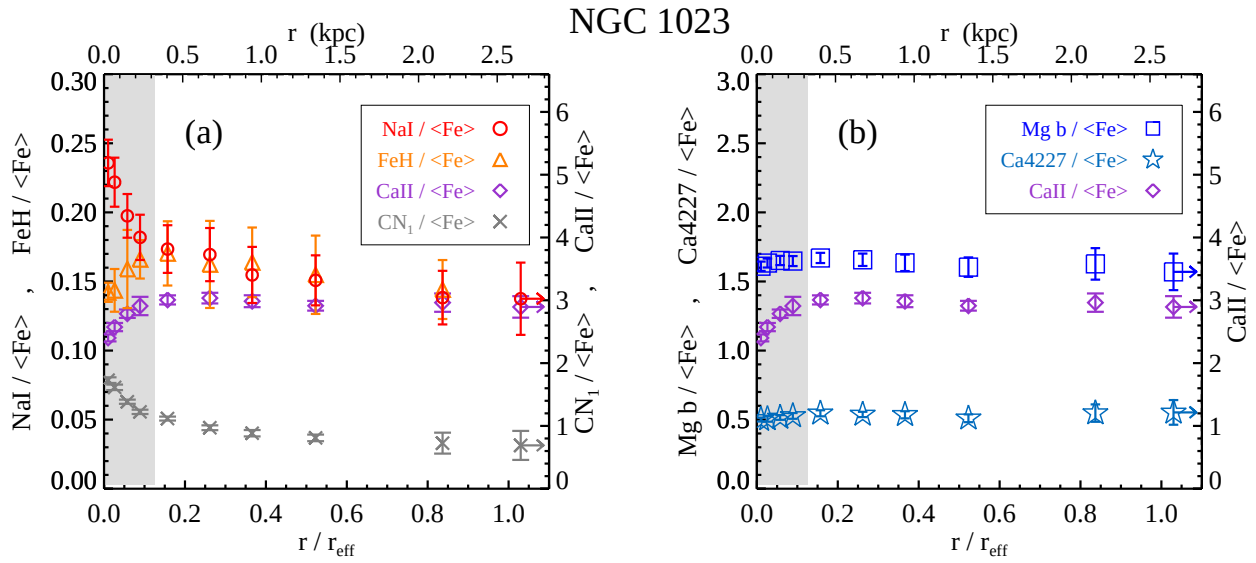

Figure 8. *Left:* ratio of IMF-sensitive indices (Na I, Ca II, and FeH) to ⟨Fe⟩, as a function of radius in NGC 1023. *Right:* ratio of α-element indices (Mg b, Ca4227, and Ca II) to ⟨Fe⟩. The spatial binning is the same as Figures 5-6, but plotted on a linear scale. The outermost spatial bin in each panel extends to $1.6\,r_{\rm eff}$. The grey shaded area indicates the scale of the single-aperture measurements by van Dokkum & Conroy (2012).

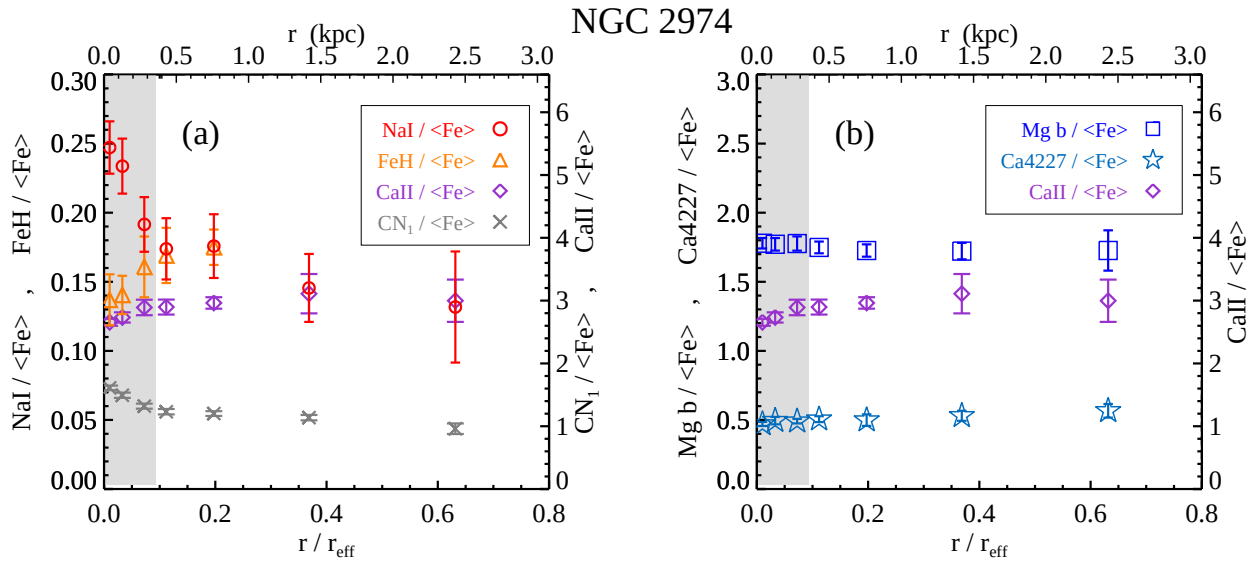

Figure 9. Same as Figure 8, for NGC 2974. The outermost spatial bin extends to $0.8\,r_{\rm eff}$.

simplifies our physical interpretation of gradients in other spectral indices.

We next turn to two absorption indices that depart from the trend of gradual radial decline: Na I and CN_1. As illustrated in Figure 7, the Na I index exhibits a much steeper gradient than other features in the central few hundred pc of each galaxy. CN_1 is the only feature showing similar radial variation to Na I (Figure 7b).

6.1.1. *IMF vs. Sodium Abundance Variations*

The Na I feature is primarily sensitive to surface temperature, surface gravity, and sodium abundance. The second effect makes it a strongly dwarf-sensitive feature in uniformly old stellar populations. Thus it is tempting to interpret our observations as a steep gradient from a bottom-heavy IMF at the galaxy center to a shallower IMF slope at $r \gtrsim 0.1\,r_{\rm eff}$ ($\sim$ 300 pc). However, this interpretation is at odds with the relatively mild decline in FeH and the opposing behavior of Na I/⟨Fe⟩ and FeH/⟨Fe⟩. The bTiO index also varies less steeply than Na I, although its strong temperature-sensitivity and the overlapping Mg4780 line leave some doubt over whether it is a valid IMF indicator (e.g., Serven et al. 2005; La Barbera et al. 2013; Spiniello et al. 2014). In addition to conventional IMF variations, CvD12 experimented with SPS models and determined that Na I could be strengthened by decreasing the number of horizontal branch and asymptotic giant branch (AGB) stars, or the

number of extremely cool giants (M7III). Yet both of these effects substantially weaken the TiO0.89 feature, which we observe to be nearly constant over the radii where Na I varies most steeply.

This leaves sodium abundance as the primary suspect for the steep variation of the Na I feature inside $\sim 0.1\,r_{\rm eff}$. Due to its prominent role as an electron donor, sodium impacts other features via the atmospheric electron pressure. In particular, an increase in [Na/Fe] will drive a mild decrease in ionized calcium (CvD12). This is qualitatively consistent with the flattening we observe in the Ca II index near the center of NGC 1023 and NGC 2974, and the corresponding decline in Ca II/$\langle$Fe$\rangle$ and Ca II/Ca4227. However, there are discrepancies between our observed Ca II strengths at all radii and SPS model predictions by CvD12. We discuss this further in §6.1.5.

Spatially resolved measurements of the Na D feature near 5890 Å would provide valuable evidence for or against gradients in [Na/Fe]. Unfortunately, our settings for LRIS did not cover Na D in NGC 1023 or NGC 2974. Jeong et al. (2013) constructed a stacked SDSS spectrum of early-type galaxies with strong Na D absorption and reported that the Na D line strength requires super-solar [Na/Fe] as well as [Z/H], with IMF slope having a relatively minor effect on the Na D feature. While their analysis provides circumstantial evidence in favor of [Na/Fe] driving trends in Na I, their single stack including galaxies with $\sigma \sim$ 150-300 km s^{-1} may wash over competing trends across the galaxy population.

Sodium is produced primarily through the Ne-Na chain, which can be activated during core burning in massive stars (e.g., Woosley & Weaver 1995; Decressin et al. 2007; Kobayashi et al. 2006, 2011) or at the base of the convective envelope in intermediate-mass AGB stars, a process known as hot bottom burning (e.g, Cottrell & Da Costa 1981; Denisenkov & Denisenkova 1990; Ventura & D'Antona 2008a,b; Karakas 2010). Although the dredge-up of heavy elements to the outer envelope of AGB stars is most efficient at low metallicities, solar-metallicity AGB stars may still produce and eject non-negligible quantities of sodium (e.g., Mowlavi 1999; Karakas et al. 2002; Herwig 2005).

6.1.2. *Nitrogen Abundance*

CN_1 is sensitive to carbon and nitrogen abundance. Our other carbon-sensitive feature, $C_2$4668, does not decline as steeply as CN_1, and both features are insensitive to IMF variations (see Figure 13 of CvD12). Since other indices do not reflect steep variations in [Z/H] or [α/Fe], we tentatively interpret the trend in CN_1 as a decrease in nitrogen abundance from $r = 0$ to $r \sim 0.1\,r_{\rm eff}$.

Nitrogen is produced via the CN cycle. Whereas primary nitrogen production is driven by the mixture of hydrogen- and helium-burning regions in the first generation of stars, the nitrogen abundance of moderate- and high-metallicity stellar populations is dominated by secondary production from later generations whose interiors are already seeded with carbon. Similar to sodium, nitrogen production may occur in the cores of massive stars or in AGB stellar envelopes (e.g., Renzini & Voli 1981; Woosley & Weaver 1995; Chiappini et al. 2003; Ventura & D'Antona 2008a,b, 2009). In particular, models of fast-rotating massive stars can boost CNO yields by mixing the hydrogen shell and helium-burning core, and observations of [N/Fe] in the Galactic disk and halo – including globular clusters ranging from [Fe/H] ~ -2.5 to [Fe/H] ~ -0.5 – are consistent with contributions from both massive stars and AGB stars (e.g., Meynet & Maeder 2002a,b; Chiappini et al. 2005; Hirchi 2007; cf. Cohen et al. 2005).

6.1.3. *Abundance Ratios in Composite Stellar Populations*

The stellar populations of early-type galaxies are typically old, with high metallicities resulting from multiple generations of star formation and interstellar medium (ISM) enrichment in a deep potential well. Their high [α/Fe] ratios could arise from short star formation timescales or a top-heavy IMF, both of which rapidly seed the ISM with α-process elements via Type II supernovae (e.g., Thomas et al. 1999, 2005). Here we briefly explore scenarios that could yield an excess of sodium and nitrogen in the centers of early type galaxies, with steep abundance gradients to larger radii.

The most straightforward explanation for excess sodium and nitrogen is a larger fraction of the stars responsible for producing these elements. This could be the direct result of a shallow (top-heavy) IMF above $\sim 10\,M_\odot$ if sodium and nitrogen are produced in stellar cores, or above $\sim 3\,M_\odot$ if AGB stars are key contributors. Production by AGB stars especially provides opportunities for [Na/Fe] and [N/Fe] to exceed [Mg/Fe] (e.g., Lecureur et al. 2007; Ventura & D'Antona 2008b). The form of the IMF at high densities is an ongoing challenge for models of star formation, and may be especially sensitive to the initial gas density structure and the role of turbulence in driving fragmentation (e.g., Chabrier et al. 2014; Krumholz 2014).

Another factor in the observed excesses is the amount of enriched stellar ejecta accreted onto existing and newly forming stars, during the peak of star formation. For instance, the high stellar densities in globular clusters allow for prolific accretion onto existing stars, as long as the cluster is massive enough to retain low-velocity ejecta (e.g., Renzini 2008; Conroy 2012; cf. Fenner et al. 2004). Nitrogen abundances in globular clusters are more exaggerated than in the extended Galactic bulge (e.g., Puzia et al. 2002; Tang et al. 2014), and an extremely high value of [Na/Fe] ≈ 1 dex has been measured in the central 15 pc of M31 (Conroy & van Dokkum 2012b). However, red giants in the Galactic bulge and Galactic globular clusters both exhibit more modest [Na/Fe], between 0 dex and +0.5 dex (e.g., Lecureur et al. 2007; Roediger et al. 2014; Johnson et al. 2014, 2015). After scaling for metallicity, our inferred abundance patterns at the centers of NGC 1023 and NGC 2974 are similar to globular clusters or ultra-compact dwarf galaxies (e.g., Cottrell & Da Costa 1981; Norris & Pilachowski 1985; Paltoglou & Norris 1989; Gratton et al. 2001; Ramírez & Cohen 2002; Strader et al. 2013). Using the deprojection procedure of Gebhardt et al. (1996), we find that the luminosity densities of NGC 1023 and NGC 2974 rise from 2-6 $L_\odot$ pc^{-3} at $0.1\,r_{\rm eff}$ to 200-400 $L_\odot$ pc^{-3} at $0.01\,r_{\rm eff}$, comparable to the average densities of some globular clusters. The rapid increase in sodium and nitrogen abundance toward these galaxies' densest regions is therefore a plausible consequence of pollution by stellar ejecta.

Compiled measurements of sodium and nitrogen in

other early-type galaxies do little to clarify the observations reported herein. Extragalactic trends in Na D/⟨Fe⟩ differ from models of elliptical galaxies or the Galactic bulge, even with overlapping ranges of Na D and ⟨Fe⟩ strength (Graves et al. 2007; Trager et al. 2008; Serven & Worthey 2010; Tang et al. 2014). Although stacked early-type galaxy spectra allegedly range from 0 dex to +1 dex in [N/Fe], the variations between different studies are larger than the population trends within any given study (e.g., Graves et al. 2007; Johansson et al. 2012; Greene et al. 2013, 2015).

6.1.4. *Is* $0.1\,r_{\rm eff}$ *a Special Radius?*

Even while the causes of excess sodium and nitrogen are murky, we have shown that the most extreme stellar populations in NGC 1023 and NGC 2974 reside in their innermost regions. In both objects, the strengths of Na I, Ca II, and CN_1 relative to other indices change abruptly near $0.1\,r_{\rm eff}$, leading us to question whether this scale marks a transition in the galaxy's previous star formation environment, or a structural landmark from the assembly of distinct progenitors. Seeking supporting evidence for unique behavior at $0.1\,r_{\rm eff}$, we have examined *Hubble Space Telescope* photometry from Lauer et al. (2005) to examine each galaxy's surface brightness profile, $V-I$ color, and ellipticity out to $\approx 0.2\,r_{\rm eff}$. We also examined the more extended surface brightness profiles from Krajnović et al. (2005) and Scott et al. (2009), as well as our measurements of v and σ for each radial bin. Generally speaking, neither galaxy exhibits an abrupt feature near $0.1\,r_{\rm eff}$ in its stellar kinematics or broadband light. In NGC 2974, σ is the dominant kinematic component inside $0.1\,r_{\rm eff}$, whereas rotational v dominates beyond $0.2\,r_{\rm eff}$. NGC 2974 also has a central dust feature, which intersects the major axis near $0.05\,r_{\rm eff}$. However, the absence of similar features in NGC 1023 suggests that they are not closely connected to the sharp abundance variations.

6.1.5. *Tension with SPS Models*

To complement our qualitative interpretation of the line index gradients in NGC 1023 and NGC 2974, we compare our measurements to the index-index plots presented by CvD12 (their Figures 12-16), which represent simplified predictions from their SPS models. Although such a comparison does not fully capture the covariance between different stellar population properties, we wish to highlight cases where our full range of measured index values differs from the model predictions. The index values from CvD12 correspond to the native resolution of their models: $\sigma = 64\,{\rm km\,s^{-1}}$. To avoid biases in our comparison, we have convolved a low-σ spectrum from the outer regions of NGC 1023 with a range of velocity kernels, such that the final σ ranges from 95 $\rm km\,s^{-1}$ to 350 $\rm km\,s^{-1}$. We then assess each line index as a function of σ, extrapolate the trend back to $64\,{\rm km\,s^{-1}}$, and apply a correction (relative to σ = 230-245 $\rm km\,s^{-1}$ as presented above) to our measurements at all radii. We also consider the effects of total metallicity and α-enhancement on individual line indices, based on the trends outlined by CvD12 and our central values of [Z/H] $\approx +0.1$ and [α/Fe] $\approx +0.2$.

After adjusting our index values for σ, [Z/H], and [α/Fe], we find that the ⟨Fe⟩, Ca4227, and Ca II indices are substantially weaker than the range of solar-metallicity predictions from CvD12. Our adjusted ⟨Fe⟩ indices range from 2.5-3.5 Å in NGC 1023 and 2.2-2.9 Å in NGC 2974. With the exception of the central ~ 100 pc in NGC 1023, these values are lower than even the young (3 Gyr) stellar population predictions from CvD12 (their Figure 12). Other empirical compilations of iron indices in early-type galaxies are consistent with our measured values (e.g., Thomas et al. 2005; Kuntschner et al. 2006).

Both of our calcium indices fall outside the range of predictions in Figure 13 of CvD12: for solar abundances, they predict Ca4227 $\approx$ 1.5-2.3 Å (varying with age), and Ca II $\approx$ 7.0-8.1 Å (varying with IMF). In comparison, our adjusted indices range from 0.3-0.8 Å for Ca4227 and 4.8-6.6 Å for Ca II. Although sodium abundance can be a factor in diminishing the Ca II index, CvD12 predict a weaker dependence – 1.6% decrease in Ca II for an increase of 0.3 dex in [Na/Fe] – than could likely explain the average offset between our measurements and the model predictions. Superficially, the single-aperture measurements of Ca II by Cenarro et al. (2003) and La Barbera et al. (2013) appear to match the predicted range by CvD12. However, the Ca II index can be impacted significantly by [α/Fe], and La Barbera et al. (2013) have noted discrepancies between their α-element corrections for Ca II and the predicted trend by CvD12.

Just as we observe puzzling behavior in Na I and FeH at $r < 0.1\,r_{\rm eff}$, our adjusted values for these indices correspond to different predictions in the CvD12 models (their Figure 12). Our adjusted FeH measurements range from $\approx$ 0.4-0.5 Å, qualitatively similar to the CvD12 predictions for a Chabrier IMF. Meanwhile, we find an adjusted range of 0.5-1.2 Å for Na I. The CvD12 predictions for a Salpeter IMF correspond to the low end of this range, matching our data near $r_{\rm eff}$, while even steeper IMFs strain to match our central Na I measurements. Alternatively, sodium enhancement in excess of [Na/Fe] = +1 could reproduce our central Na I measurements while maintaining a Chabrier IMF.

6.2. *Other Reports of IMF-Sensitive Index Gradients*

To date, few studies have sought to measure IMF gradients within individual early-type galaxies. Martín-Navarro et al. (2015a) have measured gradients in IMF-sensitive features in three galaxies, using long-slit data covering 4500-10,000 Å. Near the centers of their two high-mass galaxies, NGC 4552 and NGC 5557, they find that $\rm Na\,I_{SDSS}$ varies steeply relative to the total metallicity indicator [MgFe]′, similar to the trends we find above. Their lower-mass object, NGC 4387, shows very little radial variation in $\rm Na\,I_{SDSS}$ or in inferred stellar population properties, aside from total metallicity. Whereas we have carefully accounted for telluric absorption near 8190 Å (see §3.2 and Appendix A.3), Martín-Navarro et al. (2015a) place less confidence in their telluric correction and exclude the $\rm Na\,I_{SDSS}$ index from their SPS models. They do not measure the FeH feature, and telluric emission restricts their assessment of the Ca II feature to the second line in the triplet. However, they observe and model other features between 5800 Å and 6400 Å that we do not access with LRIS: most notably the Na D index and the temperature- and

gravity-sensitive indices TiO_1 and TiO_2.

Martín-Navarro et al. (2015a) have reported a strong IMF gradient in NGC 4552, such that the central IMF (resolved to $\sim 0.1\,r_{\rm eff}$ or ~ 300 pc) is very bottom-heavy whereas the IMF at $0.7\,r_{\rm eff}$ is nearly consistent with the Kroupa form. They argue against a gradient in [Na/Fe] based on measurements of the Na I_{SDSS} and Na D indices, which exhibit similar gradients in NGC 4552 but have different sensitivities to [Na/H] (CvD12). While the combined coverage of Na D and Na I provides useful leverage, the modeling approach of Martín-Navarro et al. (2015a) warrants caution: they fit their selected line indices to SPS models by Vazdekis et al. (2012), after applying correction factors to adjust the measured indices from inferred [α/Fe] to solar abundances. The overt dependence on [α/Fe] is particularly troubling for NGC 4552, where the strong [α/Fe] gradient reported by Martín-Navarro et al. (2015a) conflicts with measurements by Kuntschner et al. (2010) and with the typical trend of flat [α/Fe] in early-type galaxies.

Using the the same modeling approach, Martín-Navarro et al. (2015b) reported a bottom-heavy IMF out to $\geq 1.5\,r_{\rm eff}$ in the compact, high-σ galaxy NGC 1277, with a mild trend toward an even bottom-heavier IMF in the central $0.5\,r_{\rm eff}$ (600 pc). For this object, Martín-Navarro et al. (2015b) found strong gradients in Na I_{SDSS}, Na D, and metallicity, compared to relatively weak trends in TiO_1, TiO_2, and [Mg/Fe]. The results for NGC 1277 agree qualitatively with our observations of NGC 1023 and NGC 2974 on similar radial scales, and with widespread trends in [Z/H] and [α/Fe] (e.g., Tamura et al. 2000; Weijmans et al. 2009; Greene et al. 2013, 2015). Finally, Martín-Navarro et al. (2015c) have presented data from 24 galaxies in the CALIFA survey (Sánchez et al. 2012), binning each galaxy into several elliptical annuli. Although they find a significant correlation between the inferred IMF slope and metallicity of each spectrum, they do not compare any measurements directly with r. We therefore cannot assess whether galaxies in the CALIFA sample contain IMF or abundance gradients at the spatial scales we have probed for NGC 1023 and NGC 2974.

Elsewhere, La Barbera et al. (2013) assessed stacked spectra from SDSS and noted that the individual galaxy spectra enclosed varying fractions of $r_{\rm eff}$. They subdivided two of their stacked spectra ($\sigma = 100\,{\rm km\,s^{-1}}$ and $\sigma = 200\,{\rm km\,s^{-1}}$) into narrow bins of $r/\,r_{\rm eff}$, and found minimal variations in the strengths of TiO_1, TiO_2, and Na I_{SDSS} from aperture sizes of $0.3\,r_{\rm eff}$ to $1.4\,r_{\rm eff}$. In other words, their $\sigma = 200\,{\rm km\,s^{-1}}$ stack exhibited stronger IMF-sensitive features at all enclosed radii. Our interpretation of abundance-driven gradients in two early-type galaxies is consistent with the absence of IMF gradients in SDSS stacks. Yet our finding that the steepest gradients occur well inside $0.3\,r_{\rm eff}$ also might contribute to the spatially invariant trends reported by La Barbera et al. (2013).

7. CONCLUSION

We have used Keck/LRIS to analyze optical and near-infrared stellar absorption features along the major axis of two massive early-type galaxies. We have measured 13 line indices for species of H, C_2, CN, Na, Mg, Ca, TiO, Fe, and FeH, from spatially resolved spectra covering 3100-5560 Å and 7500-10,800 Å. We have examined each index on scales $\sim$ 100 pc ($1''$) near the center of each galaxy, and in larger bins extending to 4.0 kpc ($75''$ or $1.6\,r_{\rm eff}$) for NGC 1023 and 3.0 kpc ($30''$ or $0.8\,r_{\rm eff}$) for NGC 2974.

In both galaxies, the radial declines in the $\langle$Fe$\rangle$ index and multiple Mg and Ca indices suggest an overall metallicity gradient and nearly constant, enhanced [Mg/Fe] with radius, matching widely observed trends for massive early-type galaxies. However, the Na I index at 8190 Å and the CN_1 index at 4160 Å exhibit significantly steeper gradients, particularly at $r < 0.1\,r_{\rm eff}$, or $r < 300$ pc. The FeH index at 9915 Å mirrors the radial decline of Mg and Ca indices, rather than the steep decline in Na I. The data presented herein are the first to track FeH as a function of radius, and to demonstrate discrepant behavior between Na I and FeH, even while both indices are sensitive to cool dwarf stars.

We interpret the steep gradients in the Na I and CN_1 indices as reflecting a rapid decline in [Na/Fe] and [N/Fe] over the central $\sim$ 300 pc of each galaxy. This is consistent with observations of correlated sodium and nitrogen abundances in other systems, although prior investigations have not assessed sodium or nitrogen gradients on sub-kpc scales in early-type galaxies. On similar scales, the Ca II index declines relative to $\langle$Fe$\rangle$ and other Mg and Ca indices, to a degree that would require a very strong gradient in [Na/Fe] if our interpretation is to match models by CvD12. Our assertion that IMF gradients do not drive the radial variations in the Na I and Ca II indices agrees with analysis of stacked galaxy spectra from SDSS (La Barbera et al. 2013), but contradicts the analysis by Martín-Navarro et al. (2015a,c) of radial trends in several other massive ellipticals.

Our study poses a number of outstanding issues, to be pursued as future work. As we have emphasized above, the physical properties of stellar populations are highly degenerate with individual line indices, and some of the trends we have presented – most notably the relative variations in Na I, FeH, and $\langle$Fe$\rangle$ – defy simple qualitative arguments. Stellar population synthesis modeling will allow for more robust interpretations of the physical trends in NGC 1023 and NGC 2974. At the same time, one must be mindful of ongoing discrepancies between observed spectral features and model predictions. As one example, we have noted the relatively high $\langle$Fe$\rangle$, Ca4227, and Ca II values predicted by models from CvD12. Finally, our search for radial IMF trends within two galaxies cannot fully inform claims of IMF variation over a large range of integrated galaxy properties. To this end we have observed five additional galaxies spanning $\sigma \sim$ 140-400 ${\rm km\,s^{-1}}$, approaching the range explored by survey-driven investigations of IMF variation. These objects will also strengthen our understanding of internal trends near $0.1\,r_{\rm eff}$ and clarify whether this scale truly marks a transition point for star formation physics in galaxies.

We thank Daniel Perley for providing access to his pipeline for LRIS data reduction, and Pieter van Dokkum and Charlie Conroy for publishing a straightforward blueprint of their observing strategy. Marc Kassis, Luca Rizzi, and Hien Tran at W. M. Keck Observatory pro-

vided essential support for conducting LRIS observations. NJM is supported by the Beatrice Watson Parrent Fellowship. AWM is supported by the Harlan J. Smith Fellowship. Finally, we recognize the sacredness and cultural significance of Maunakea to indigenous Hawaiians, who have honored the land long before and indeed since the construction of modern astronomical facilities. We hold great privilege and responsibility in using the Maunakea summit for scientific inquiry.

APPENDIX

A: SYSTEMATICS IN LINE INDEX MEASUREMENTS

Herein we derive our total systematic error $\epsilon_{\rm sys}$, which we have included above in §4.1. Figures 5 and 6 above include all systematic terms, while Figures 7-9 include all systematic terms except for the telluric absorption error in Na I.

A.1: Kinematic Corrections

In order to make an unbiased comparison between absorption line strengths at different radii, each spectrum within a single galaxy must be shifted to the same rest frame and convolved to the same velocity dispersion. For each spectrum, we measure v and σ using the template reconstruction procedure `pPXF` from Cappellari & Emsellem (2004). We use a subset of template spectra from the MILES library of empirical stellar spectra (Sánchez-Blázquez et al. 2006), and perform a fit over the wavelength range 3650-5400 Å. We simultaneously fit for the strengths of emission lines, assuming that gas and stars exhibit the same kinematics. Spectra on the LRIS red arm are assumed to match the kinematics derived from blue-arm data for the same spatial bins.

At high S/N, uncertainties in v and σ are dominated by systematic errors, particularly from template libraries that do not fully reproduce a galaxy's underlying stellar population. For this work, we do not attempt to directly assess our systematic errors in kinematic moments, but rather test the variation in line index strengths over a conservative range of assumed v and σ. Previous investigations using similar wavelength coverage and a variety of stellar templates have found total errors $\lesssim 10\,{\rm km\,s^{-1}}$ in v and $\lesssim 20\,{\rm km\,s^{-1}}$ in σ (Barth et al. 2002; Cappellari & Emsellem 2004). For the SAURON galaxy sample, Emsellem et al. (2004) found scatter of 15-18 $\rm km\,s^{-1}$ in comparisons between their `pPXF`-based measurements of σ and previous σ values in the literature. For our trials, we adopt the conservative assumption that v and σ each have errors of $20\,{\rm km\,s^{-1}}$. We have run `pPXF` using an alternative subset of MILES stellar templates and found that the resulting variations in v and σ were well within this range.

In order to assess the kinematic error terms for each line index, we have tested five spectra from NGC 1023. The innermost spectrum spans radii from $0.5''$ to $2.0''$, with $S/N = 119$ over the wavelength range used for the `pPXF` fit, and $\sigma = 216\,{\rm km\,s^{-1}}$. The outermost spectrum spans $50''$-$75''$ and has $S/N = 38$ and $\sigma = 94\,{\rm km\,s^{-1}}$. For a given spectrum, we perform two sets of trials wherein we vary the assumed velocity and velocity dispersion, v_0 and σ_0. In one set of trials, we fix σ_0 to the best-fit σ from `pPXF` and sample v_0 from a normal distribution with a dispersion of $20\,{\rm km\,s^{-1}}$ (centered on the best-fit v from `pPXF`). For each of 100 trials sampling v_0, we convolve the spectrum from σ_0 to $\sigma = 230\,{\rm km\,s^{-1}}$, shift to $\lambda_{\rm rest} = \lambda_{\rm obs}/(1 + v_0/c)$, and measure the absorption line indices. For each absorption feature, we define a systematic error term ϵ_{v0} as the standard deviation in index strength over all 100 trials. Our second set of trials assesses an analogous error term $\epsilon_{\sigma 0}$ by employing a nearly identical procedure whereby v_0 is held fixed and σ_0 is sampled from a normal distribution with a dispersion of $20\,{\rm km\,s^{-1}}$.

In Table 3 we present the values of ϵ_{v0} and $\epsilon_{\sigma 0}$ for 13 different line indices, averaged over our five test spectra. We make particular note of the Na I index, which is 2-3 times stronger at the galaxy center than at large radii. This index exhibits a similar absolute value of $\epsilon_{v0} \approx 0.025$ Å at all radii, while $\epsilon_{\sigma 0}$ scales approximately linearly with the index strength. The trends in ϵ_{v0} and $\epsilon_{\sigma 0}$ for both galaxies' Na I indices are illustrated in Figure 10. Figures 11 and 12 show individual spectra of the Na I region for NGC 1023, with variations in v_0 and σ_0 and the resulting smoothed spectra. Although the inner

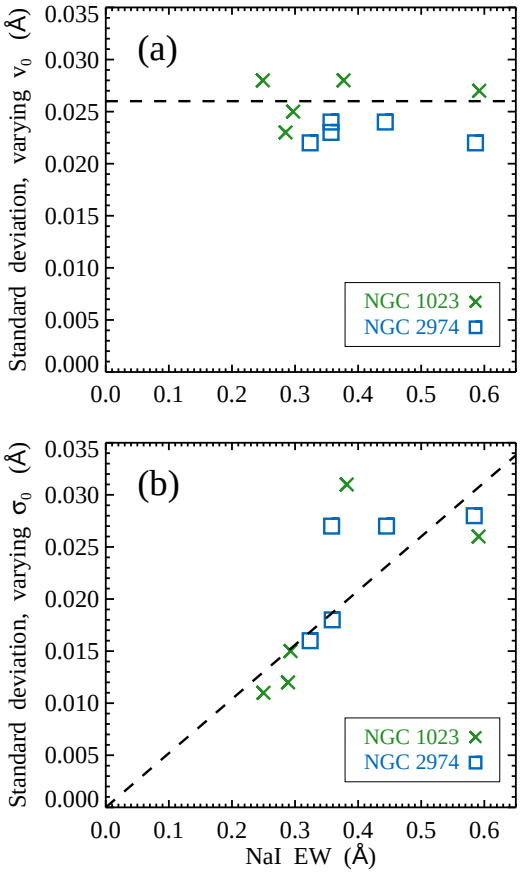

Figure 10. *Top:* Error in Na I feature strength for test spectra in NGC 1023 and NGC 2974, where each spectrum was shifted to rest wavelengths from a range of velocities v_0. Uncertainty in the systemic velocity produces a nearly constant error over a large range of line depths. The dashed line corresponds to an average error of 0.025 Å, from trials sampling a conservative distribution of v_0. *Bottom:* error in Na I strength for test spectra convolved to $230\,{\rm km\,s^{-1}}$ (NGC 1023) or $245\,{\rm km\,s^{-1}}$ (NGC 2974) from a range of initial velocity dispersions σ_0. Uncertainty in the measured velocity dispersion produces an error that increases with line depth. The dashed line corresponds to an error of 5.5%.

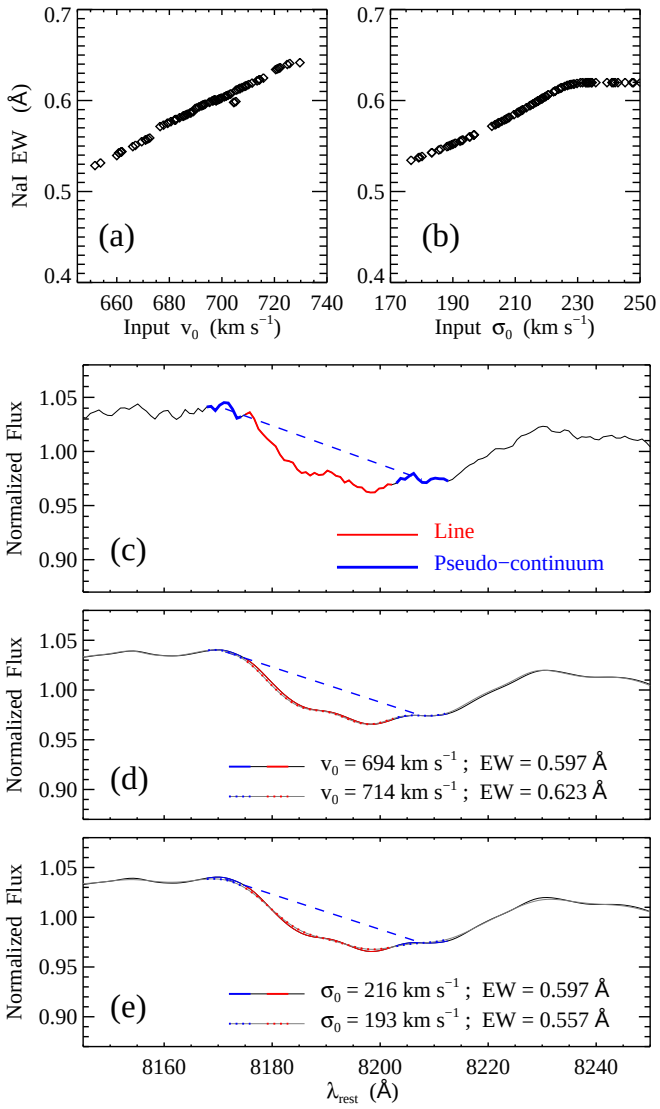

Figure 11. (a) line strength of Na I feature vs. input systemic velocity (v_0), for a spectrum covering major-axis radii from $+0.5''$ to $+2.0''$ in NGC 1023. (b) Na I line strength vs. input velocity dispersion (σ_0). In each case, the spectrum is convolved from σ_0 to $\sigma = 230\,\mathrm{km\,s^{-1}}$ before measuring the line index. (c) rest-frame spectrum of the Na I feature, before convolution to $\sigma = 230\,\mathrm{km\,s^{-1}}$. The red segment indicates the Na I line region, and the blue segments indicate the pseudo-continuum regions. The blue dashed line is the linear fit to the pseudo-continuum, used in the index measurement. (d) rest-frame spectrum at two separate velocity shifts. (e) rest-frame spectrum convolved to 230 $\mathrm{km\,s^{-1}}$ from two separate σ_0 values.

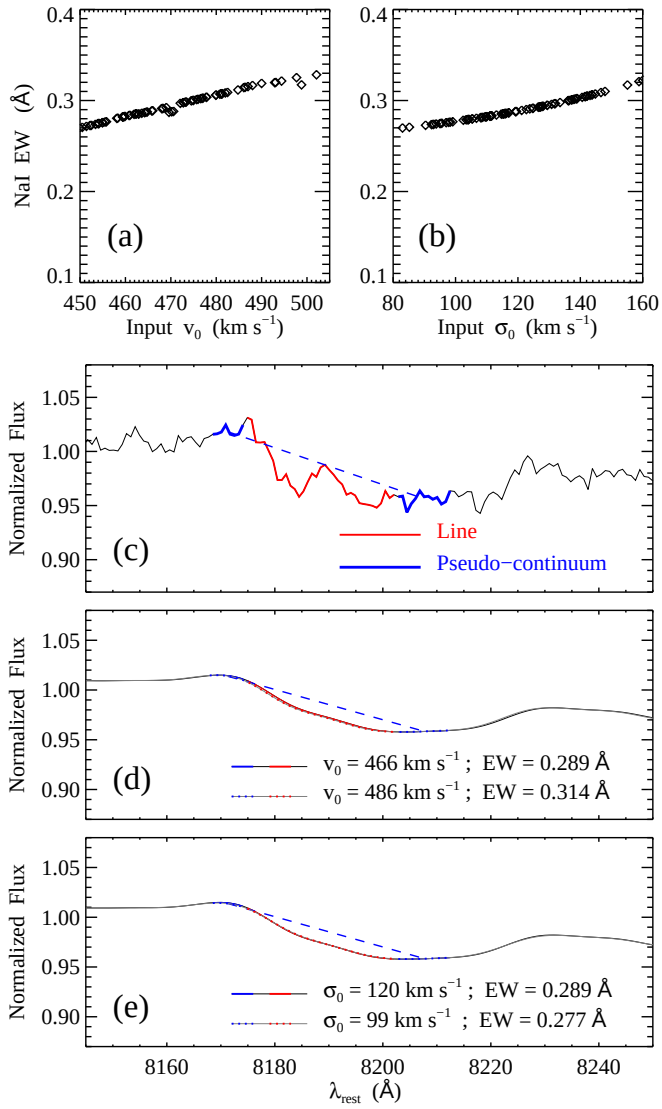

Figure 12. Panels are the same as Figure 11. This spectrum spans major-axis radii from $-50''$ to $-30''$ in NGC 1023. The velocity dispersion is smaller than the central spectrum in Figure 11, and the Na I line is significantly weaker.

spectrum (Figure 11) has a much deeper Na I feature and much larger intrinsic σ, the change in index strength with respect to v_0 is similar to the outer spectrum (Figure 12).

As indicated in Table 3, systematic errors from kinematic fitting are typically $\sim$ 1%-5% of the line index strength. In cases of low statistical noise, the ϵ_{v0} and/or $\epsilon_{\sigma 0}$ term is comparable to the level of random variance between different data subsets. This is true for index measurements based on high-S/N spectra near the center of each galaxy, and even toward large radii for the Fe, Mg b, and Ca II features. On the other hand, the Na I and MgI0.88 features are relatively sensitive to the velocity shift and broadening of the underlying spectrum, such that the kinematic error terms make a substantial contribution to the overall error budget even when S/N is modest.

A.2: Contamination from Emission Lines

Emission lines from warm gas are visible contaminants in our spectra throughout NGC 2974, and also may be present at low levels in NGC 1023. We have experimented with two well-known routines to remove the emission component and assess the underlying stellar absorption features: `pPXF` by Cappellari & Emsellem (2004) and `GANDALF` by Sarzi et al. (2006). In addition to the stellar template library used to fit a galaxy spectrum, `pPXF` supports Gaussian emission line templates at the rest wavelengths of several gas species. The strength of each emission line is varied freely, while the emission line kinematics (v and σ) are assumed to match the stellar

Table 3
Systematic Errors in Line Indices

Index	Error from v_0	Error from σ_0	Telluric absorption error NGC 1023 / NGC 2974	Error from emission lines NGC 1023 / NGC 2974	Adopted systematic error NGC 1023 / NGC 2974
CN_1	0.4 %	0.9 %	–	0.9 % / 1.4 %	1.3 % / 1.7 %
Ca4227	1.3 %	1.9 %	–	–	2.3 %
$C_2$4668	0.4 %	0.4 %	–	– / 0.4 %	0.6 % / 0.7 %
bTiO	4.1 %	1.4 %	–	– / 5.2 %	4.3 % / 6.8 %
Hβ	1.4 %	0.2 %	–	6.0 % / 6.0 %	6.2 % / 6.2 %
Mg b	0.4 %	0.9 %	–	0.7 % / 1.0 %	1.2 % / 1.4 %
Fe5270	0.3 %	1.4 %	–	–	1.4 %
Fe5335	0.7 %	2.7 %	–	–	2.8 %
NaI	0.025 Å	5.5 %	15.1 % / 5.9 %	–	$\left[0.025^2 + (0.055^2 + 0.151^2)\,\mathrm{EW}^2_{\mathrm{Na\,I}}\right]^{1/2}$ Å $\left[0.025^2 + (0.055^2 + 0.059^2)\,\mathrm{EW}^2_{\mathrm{Na\,I}}\right]^{1/2}$ Å
CaII	1.1 %	0.7 %	–	–	1.3 %
MgI0.88	2.1 %	5.6 %	–	–	6.0 %
TiO0.89	0.03 %	0.06 %	–	–	0.07 %
FeH	2.6 %	2.3 %	–	–	3.5 %

Notes: In most cases the adopted systematic error is $\epsilon_{\rm sys} = (\epsilon^2_{v0} + \epsilon^2_{\sigma 0})^{1/2}$, where ϵ_{v0} and $\epsilon_{\sigma 0}$ are the error terms from v_0 and σ_0. For indices impacted by telluric absorption or galaxy emission lines, the adopted systematic error is $\epsilon_{\rm sys} = (\epsilon^2_{v0}+\epsilon^2_{\sigma 0}+\epsilon^2_{\rm tel}+\epsilon^2_{\rm gas})^{1/2}$, where $\epsilon_{\rm tel}$ is the error resulting from uncertainties in the atmospheric transmission spectrum, and $\epsilon_{\rm gas}$ is the error derived from different settings for emission line removal. For Na I, the adopted systematic error ranges from 6.6% of the equivalent width near the galaxy center to 13% of the equivalent width at large radii.

kinematics. Using the output template data provided by `pPXF`, we separate the stellar template and emission line components, and subtract the sum of the emission lines from our original galaxy spectrum. For NGC 2974, this is performed in the same run where we measure v and σ. For NGC 1023, our default assumption in measuring v, σ, and line indices is that the stellar absorption features are uncontaminated by gas emission. Still, we have run comparison trials with `pPXF` including emission line fits, to assess the possible effect of low-level emission on our reported line indices.

The `GANDALF` routine adds more flexibility to the emission-line fitting: the gas component(s) are permitted to have different kinematics from the stars, and the relative flux and kinematics of each emission line may either be fit freely or coupled to another line. In practice, the routine performs best when the stellar kinematics are first estimated using `pPXF` (while masking the emission lines or fixing their kinematics as above), and supplied as an initial guess for the subsequent `GANDALF` fit. We have used `GANDALF` successfully for NGC 2974, whose strong emission lines are easily recognized. As before, we isolate the emission-line component of the best-fitting spectrum and subtract it from our original galaxy spectrum. Any emission in NGC 1023 is too subtle for `GANDALF` to separate cleanly, however, and it confuses the low-order stellar continuum with a superposition of extremely broad emission lines. Therefore, we restrict our use of `GANDALF` to NGC 2974.

We find that the best-fitting emission spectrum varies for different sets of stellar templates used in `pPXF`, and with the degree to which the relative emission strengths of different species are allowed to vary in `GANDALF`. We therefore define a systematic error term $\epsilon_{\rm gas}$ as the standard deviation of trial measurements for a given absorption line index, when different settings are used for the emission line removal. For NGC 2974, the trials include two alternative stellar template libraries – each a subset of the empirical MILES library – for `pPXF`, and two settings for the relative emission line strengths in `GANDALF`. In one `GANDALF` trial the flux of each emission line is treated as a free parameter, and in the other trial we fix the relative strengths within the [OII], [OIII], [NI], and [ArIV] multiplets. In NGC 2974, Balmer emission lines impact the CN_1, bTiO, and Hβ absorption features. For Hβ we find that $\epsilon_{\rm gas} \approx 6\%$ of the absorption line strength, and bTiO is impacted at the $\approx 5\%$ level as a result of Hβ contaminating the red pseudo-continuum. The Mg b and $C_2$4668 indices exhibit small systematic errors from [NI] and [ArIV] contamination, respectively. For the average index measurements presented in §5 and Figures 6-9 we have adopted `pPXF` as our default tool for emission line removal, as we find it performs better at distinguishing between relatively narrow emission lines and broad variations in the galaxy continuum relative to the stellar templates.

For NGC 1023 we determine $\epsilon_{\rm gas}$ using two trials: a `pPXF` trial with our default template library, and a trial with no emission line fitting. A third trial with an alternative template library for `pPXF` does not differ substantially for NGC 1023, and we exclude it so as not to dilute $\epsilon_{\rm gas}$. As with NGC 2974, we find a $\approx 6\%$ impact on the Hβ index, and possible low levels of contamination for the CN_1 and Mg b absorption features.

A.3: Overlap of redshifted Na I *and telluric* H_2O

We have attempted to remove telluric absorption features from our galaxy spectra by comparing them to a grid of model atmospheric transmission spectra over the observed wavelength range 9310-9370 Å. Although

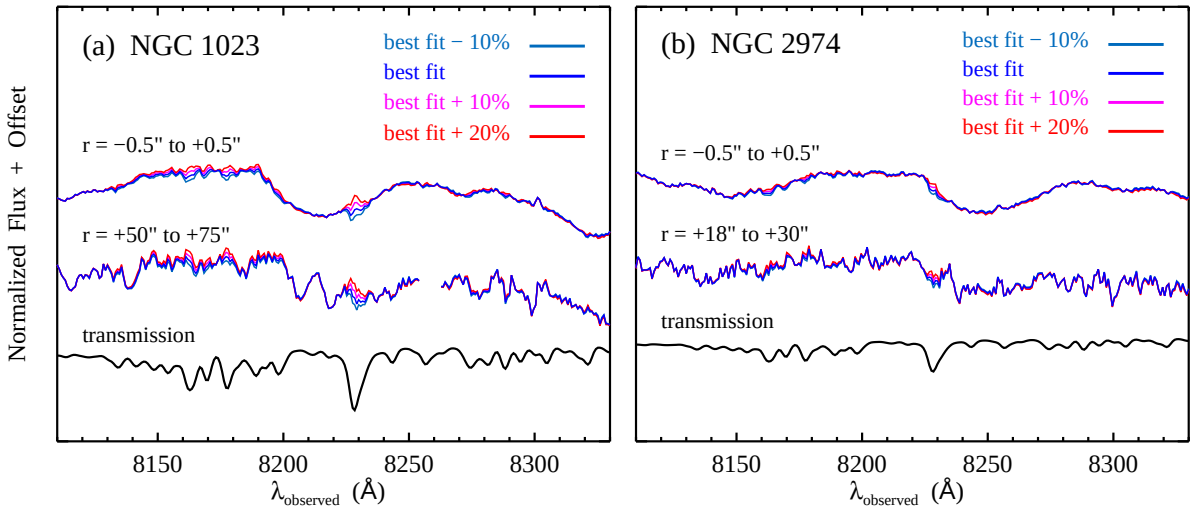

Figure 13. Galaxy spectra near the Na I absorption feature, after varying the strength of telluric absorption bands. *Left:* spectra from our central and outermost bins in NGC 1023. *Right:* spectra from our central and outermost bins in NGC 2974.

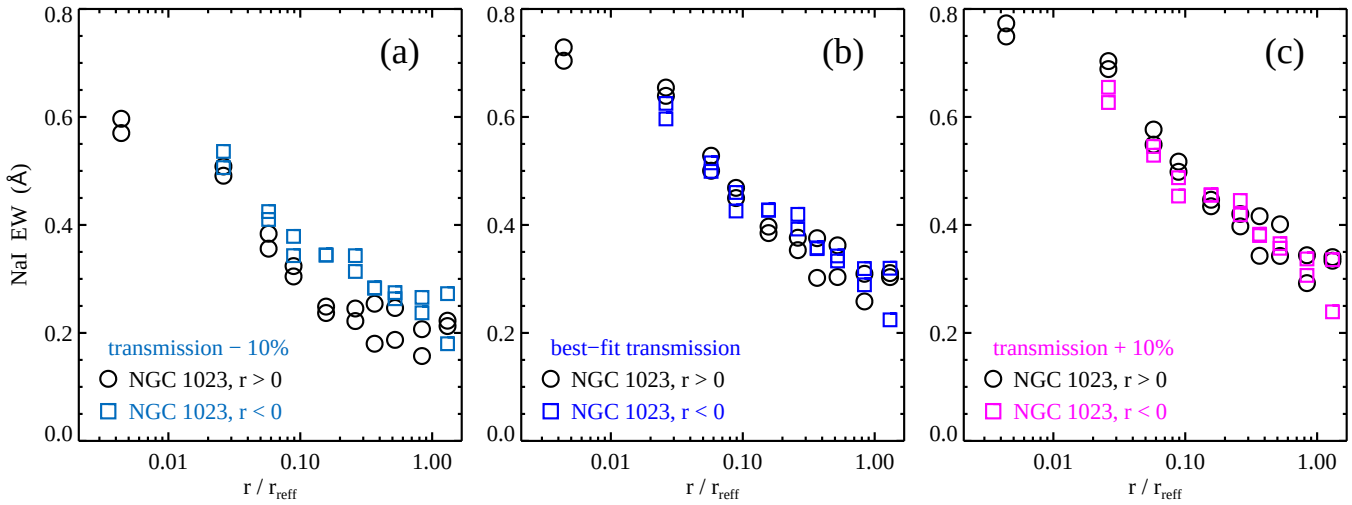

Figure 14. Comparison of Na I measurements in NGC 1023, for various levels of telluric correction. The rotation curve of the galaxy will shift stellar absorption features with respect to imperfectly corrected telluric absorption bands, driving asymmetries in the line index measurements from opposite sides of the galaxy. *Left:* Na I measurements after weakening our best-fitting atmospheric transmission spectra by 10%. *Middle:* Na I measurements using our best-fitting transmission spectra. *Right:* Na I measurements after strengthening our best-fitting transmission spectra by 10%. The middle and right panels both represent a plausible strength for telluric absorption features in our spectra, whereas the left panel exhibits clear asymmetry between opposite sides of the galaxy as the result of poor telluric correction.

our corrected spectra look reasonable by eye, we aim to quantify the level of uncertainty near the 8190Å Na I feature and the corresponding bias in our measurement of the Na I line index. To this end, we have performed trials where we multiplied the strength of our best-fitting transmission spectrum for each science exposure by values of 0.9, 1.1, and 1.2, and repeated all data processing and analysis steps starting from telluric division of individual frames. In Figure 13 we display the resulting spectra for each galaxy, from our central spatial bin and an outer spatial bin.

For NGC 1023 (Figure 13a), contamination by the deep H_2O feature at 8230 Å is visible for telluric correction of -10% and +20% relative to the best fit. Beyond a crude visual estimate of our possible error range for telluric correction, we can take advantage of the fact that NGC 1023 and NGC 2974 both have rotational velocities $\sim 200\,\mathrm{km\,s^{-1}}$, such that the Na I feature is shifted by ~ 10 Å over the length of our slit. If the Na I line or pseudo-continuum regions are severely contaminated by a telluric feature, we should see systematic differences in our index measurements from opposite sides of the galaxy. This is illustrated in Figure 14. For each panel, we have overplotted all four subsamples used to compute our random errors in the Na I index (see §4.1). For the trial where we adjusted our transmission spectra by -10% (Figure 14a), our measurements of the Na I index on opposite sides of the galaxy are clearly offset. We see similar

asymmetry for the trial with +20% adjustment, though it is not displayed in Figure 14. Our other two trials (no adjustment and +10%, corresponding to Figures 14b and 14c) both exhibit overlapping measurements from opposite sides of the galaxy and do not produce obviously poor spectra. We therefore estimate our plausible systematic error from telluric correction in terms of the difference between our Na I index measurements from these latter two trials. Specifically, we have adjusted our final Na I index measurement in each spatial bin of NGC 1023 to the average value from the two trials, and we define the 1-σ systematic error term $\epsilon_{\rm tel}$ as the percent deviation between the two trials, equal to $\frac{1}{\sqrt{2}}$ times the percent difference in index measurements.

Our random errors in each line index are derived from subsets of data spanning both sides of the galaxy (§4.1), and therefore some of the scatter in Figure 14 is already incorporated in the random error term for Na I. However, Figure 14 also exhibits a systematic offset between the three panels, indicating that poor telluric correction introduces an overall bias in addition to increased scatter from the shift in observed wavelengths of Na I. We therefore keep the $\epsilon_{\rm tel}$ term as defined above, to account for the plausible bias level from over- or under-corrected telluric features.

We observed NGC 2974 during the second half of our observing night, and telluric H_2O in our spectra is not as strong as for NGC 1023 (see Figure 13b). Yet our -10% and +20% atmospheric transmission trials once again produce offsets in the Na I index measurements from opposite sides of the galaxy. Therefore we define $\epsilon_{\rm tel}$ for NGC 2974 in the same manner as for NGC 1023, and adjust our average index values accordingly. For NGC 2974 we compute $\epsilon_{\rm tel} = 5.9\%$, versus 15.1% for NGC 1023. For both galaxies we add $\epsilon_{\rm tel}$ in quadrature with other systematic terms, as indicated in Table 3.

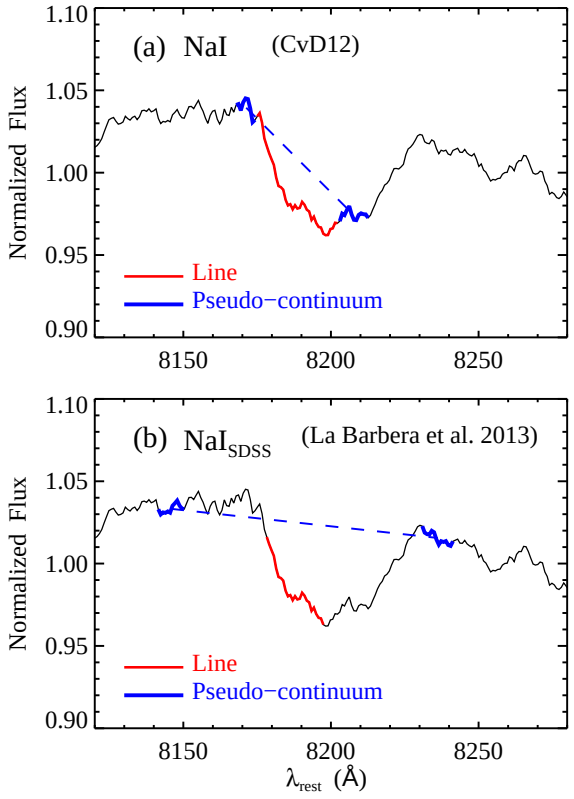

Figure 15. Comparison of the Na I and Na I$_{\rm SDSS}$ indices defined in Table 2. In each panel the red segment indicates the line region, and the blue segments indicate the pseudo-continuum regions. The blue dashed line is the linear fit to the pseudo-continuum, used in the index measurement. The example galaxy spectrum is the same as in Figure 11, prior to convolution to $\sigma = 230\,{\rm km\,s^{-1}}$.

B: ALTERNATIVE DEFINITIONS OF THE SODIUM 8190Å AND FEH WING-FORD INDICES

In recent investigations of IMF-sensitive absorption features, CvD12 and La Barbera et al. (2013) have proposed two different definitions of the Na I absorption index near 8190 Å. We compare the corresponding line and pseudo-continuum regions in Figure 15. In the version by CvD12, both pseudo-continuum regions are immediately adjacent to the line region, such that the red

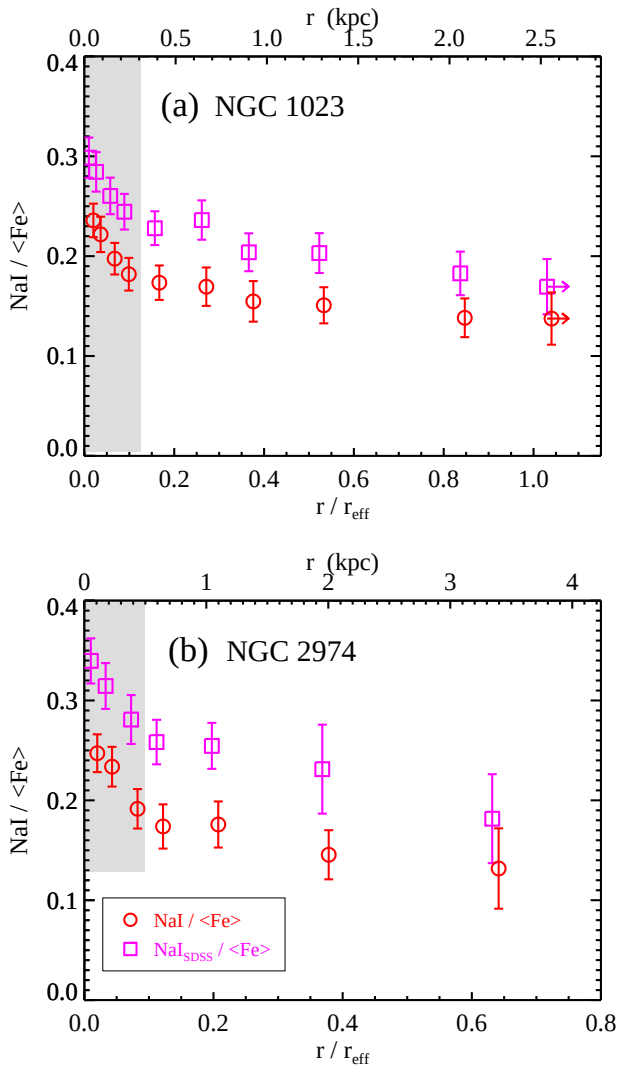

Figure 16. Ratio of Na I and Na I$_{\rm SDSS}$ to ⟨Fe⟩ as a function of radius. *Left*: NGC 1023, with the outermost spatial bin extending to $1.6\,r_{\rm eff}$. *Right:* NGC 2974, with the outermost spatial bin extending to $0.8\,r_{\rm eff}$. The grey shaded area in each panel indicates the scale of the single-aperture measurement by van Dokkum & Conroy (2012).

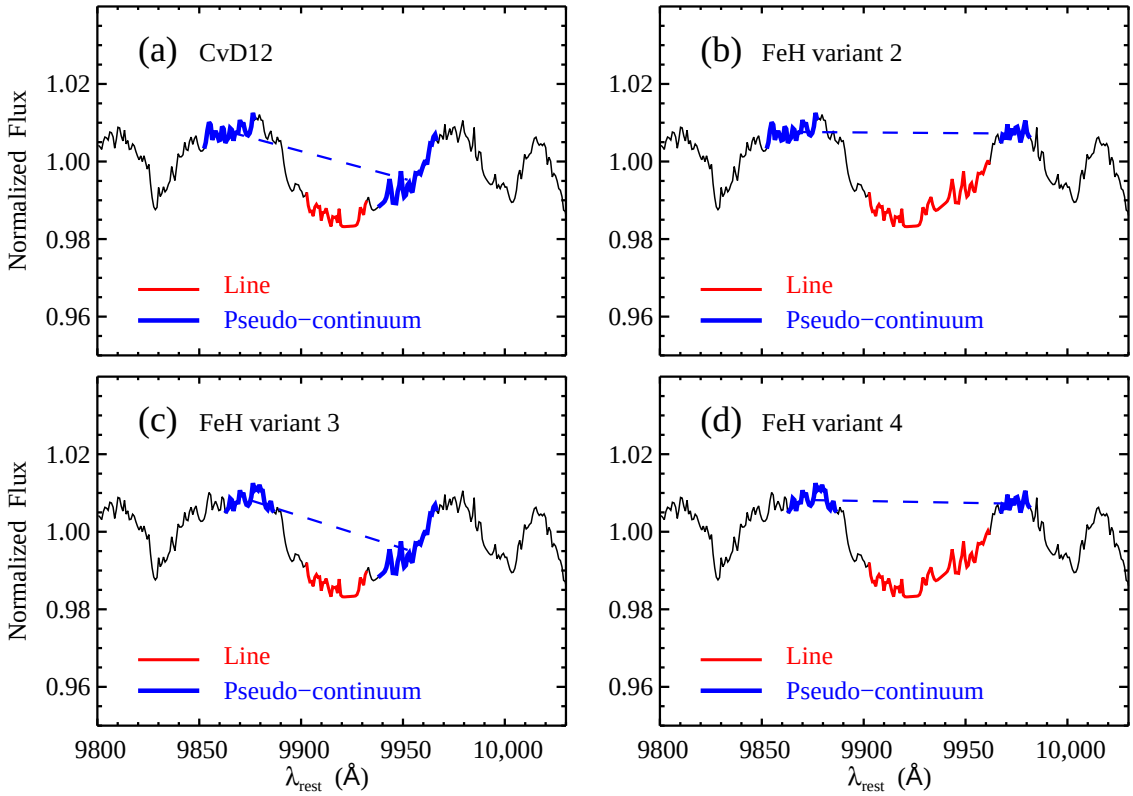

Figure 17. Comparison of the FeH index definition from CvD12 and three variants explored herein. In each panel the red segment indicates the line region, and the blue segments indicate the pseudo-continuum regions. The blue dashed line is the linear fit to the pseudo-continuum, used in the index measurement. The example galaxy spectrum is the innermost bin ($-5''$ to $+5''$) for NGC 1023, with no velocity convolution. For visualization purposes, the spectrum has been divided by a fourth-order polynomial approximating the continuum from 9800-10,050 Å.

pseudo-continuum lies directly on the overlapping TiO band. The Na I$_{\rm SDSS}$ index from La Barbera et al. (2013) defines a narrower line region and moves both pseudo-continua to regions outside the Na I+TiO blend. This generates a shallower linear fit to the continuum and produces larger equivalent widths. However, we find that the offset between our measured Na I and Na I$_{\rm SDSS}$ line strengths is nearly the same at all radii in NGC 1023 and NGC 2974. In Figure 16 we show the ratios Na I/$\langle$Fe$\rangle$ and Na I$_{\rm SDSS}$/$\langle$Fe$\rangle$ as a function of radius in NGC 1023 and NGC 2974. For both definitions, the relative strength of the sodium index rises steeply from 0.1 $r_{\rm eff}$ to the galaxy center. For all figures and discussion above, we follow the Na I index definition from CvD12.

The relative strengths of the FeH, Na I, and $\langle$Fe$\rangle$ absorption features are crucial for our interpretation of abundance versus IMF gradients in NGC 1023 and NGC 2974. The FeH index is notoriously difficult to measure, as spectra near 9900 Å suffer from bright telluric emission lines and relatively low instrumental throughput. While the Wing-Ford feature corresponds to the principal FeH bandhead in this region, the shape of the nearby pseudo-continuum is also influenced by overlapping bands of TiI, TiO, and CrH (e.g., McLean et al. 2003; Cushing et al. 2005, CvD12). To check whether our observed radial trends in FeH are sensitive to the precise placement of the line and pseudo-continuum regions, we have repeated our measurements using four variants of the index definition. These are illustrated in Figure 17. The first variant is the definition by CvD12, which we list in Table 2 and use for all analysis and figures above. In this version, the line region is defined to match the deepest part of the FeH bandhead, possibly reducing contamination from overlapping TiO. Our second variant instead uses a larger portion of the FeH trough (9902.3-9962.3 Å) and moves the red pseudo-continuum accordingly to 9967.3-9982.3 Å. The third and fourth variants match the first two, except with the blue pseudo-continuum moved from 9852.3-9877.3 Å to 9862.3-9887.3 Å.

We display the radial trends of FeH/$\langle$Fe$\rangle$ for each variant in Figure 18. None of the adopted FeH variants alter our main finding: that FeH decreases relative to $\langle$Fe$\rangle$ going from 0.1 $r_{\rm eff}$ into the center of each galaxy, and thereby opposes the trend in Na I/$\langle$Fe$\rangle$ at these same radii. Yet there is evidence of some deviation at $r > 0.5\,r_{\rm eff}$ in NGC 1023, such that the variants using the full absorption trough (variants 2 and 4) show an increase in FeH toward large r, whereas the original definition by CvD12 and our similar variant 3 show a slight decrease toward large r. This may be caused by a faint sky line near 9970 Å rest, which overlaps with the red pseudo-continuum in our full-trough variants. Traces of this line are visible in Figure 3b and for the two outermost spectra in Figure 4c.

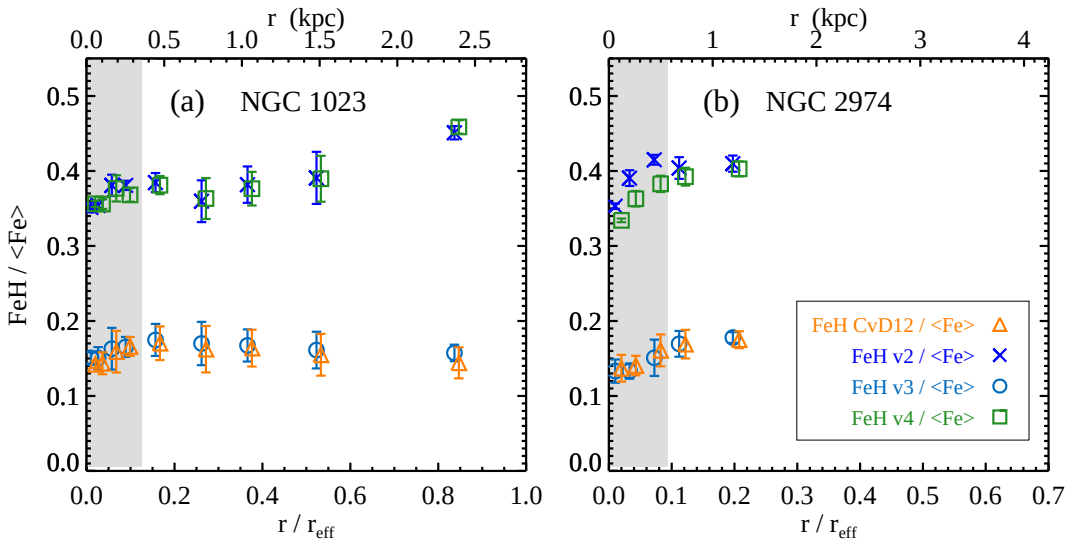

Figure 18. Ratio of FeH to ⟨Fe⟩ as a function of radius, using the four definitions of the FeH index in Figure 17. *Left*: NGC 1023, with good data for FeH extending to $1.0\,r_{\rm eff}$. *Right:* NGC 2974, with good data for FeH extending to $0.26\,r_{\rm eff}$. The grey shaded area in each panel indicates the scale of the single-aperture measurement by van Dokkum & Conroy (2012).

REFERENCES

Auger, M. W., Treu, T., Gavazzi, R., et al. 2010, ApJL, 721, L163
Barth, A. J., Ho, L. C., & Sargent, W. L. W. 2002, AJ, 124, 2607
Bastian, N., Covey, K. R., & Meyer, M. R. 2010, ARA&A, 48, 339
Behroozi, P. S., Wechsler, R. H., & Conroy, C. 2013, ApJ, 770, 57
Cappellari, M., & Emsellem, E. 2004, PASP, 116, 138
Cappellari, M., Emsellem, E., Krajnović, D., et al. 2011, MNRAS, 413, 813
Cappellari, M., McDermid, R. M., Alatalo, K., et al. 2012, Nature, 484, 485
—. 2013b, MNRAS, 432, 1862
Cenarro, A. J., Cardiel, N., Gorgas, J., et al. 2001, MNRAS, 326, 959
Cenarro, A. J., Gorgas, J., Vazdekis, A., Cardiel, N., & Peletier, R. F. 2003, MNRAS, 339, L12
Chabrier, G. 2003, PASP, 115, 763
Chabrier, G., Hennebelle, P., & Charlot, S. 2014, ApJ, 796, 75
Chiappini, C., Matteucci, F., & Ballero, S. K. 2005, A&A, 437, 429
Chiappini, C., Romano, D., & Matteucci, F. 2003, MNRAS, 339, 63
Cid Fernandes, R., Mateus, A., Sodré, L., Stasińska, G., & Gomes, J. M. 2005, MNRAS, 358, 363
Coccato, L., Gerhard, O., & Arnaboldi, M. 2010, MNRAS, 407, L26
Cohen, J. G., Briley, M. M., & Stetson, P. B. 2005, AJ, 130, 1177
Conroy, C. 2012, ApJ, 758, 21
Conroy, C., Graves, G. J., & van Dokkum, P. G. 2014, ApJ, 780, 33
Conroy, C., Gunn, J. E., & White, M. 2009, ApJ, 699, 486
Conroy, C., & van Dokkum, P. G. 2012a, ApJ, 747, 69 (CvD12)
—. 2012b, ApJ, 760, 71
Cottrell, P. L., & Da Costa, G. S. 1981, ApJL, 245, L79
Cushing, M. C., Rayner, J. T., & Vacca, W. D. 2005, ApJ, 623, 1115
Decressin, T., Meynet, G., Charbonnel, C., Prantzos, N., & Ekström, S. 2007, A&A, 464, 1029
Denisenkov, P. A., & Denisenkova, S. N. 1990, Soviet Astronomy Letters, 16, 275
Dutton, A. A., Macciò, A. V., Mendel, J. T., & Simard, L. 2013, MNRAS, 432, 2496
Dutton, A. A., Mendel, J. T., & Simard, L. 2012, MNRAS, 422, L33
Emsellem, E., Cappellari, M., Peletier, R. F., et al. 2004, MNRAS, 352, 721
Emsellem, E., Cappellari, M., Krajnović, D., et al. 2011, MNRAS, 414, 888
Faber, S. M., Friel, E. D., Burstein, D., & Gaskell, C. M. 1985, ApJS, 57, 711
Fenner, Y., Campbell, S., Karakas, A. I., Lattanzio, J. C., & Gibson, B. K. 2004, MNRAS, 353, 789
Ferreras, I., La Barbera, F., de la Rosa, I. G., et al. 2013, MNRAS, 429, L15
Gebhardt, K., Richstone, D., Ajhar, E. A., et al. 1996, AJ, 112, 105
Gratton, R. G., Bonifacio, P., Bragaglia, A., et al. 2001, A&A, 369, 87
Graves, G. J., Faber, S. M., Schiavon, R. P., & Yan, R. 2007, ApJ, 671, 243
Graves, G. J., & Schiavon, R. P. 2008, ApJS, 177, 446
Greene, J. E., Janish, R., Ma, C.-P., et al. 2015, ArXiv e-prints
Greene, J. E., Murphy, J. D., Comerford, J. M., Gebhardt, K., & Adams, J. J. 2012, ApJ, 750, 32
Greene, J. E., Murphy, J. D., Graves, G. J., et al. 2013, ApJ, 776, 64
Herwig, F. 2005, ARA&A, 43, 435
Hirschi, R. 2007, A&A, 461, 571
Hopkins, P. F., Bundy, K., Hernquist, L., Wuyts, S., & Cox, T. J. 2010, MNRAS, 401, 1099
Jeong, H., Yi, S. K., Kyeong, J., et al. 2013, ApJS, 208, 7
Johansson, J., Thomas, D., & Maraston, C. 2012, MNRAS, 421, 1908
Johnson, C. I., Rich, R. M., Kobayashi, C., Kunder, A., & Koch, A. 2014, AJ, 148, 67
Johnson, C. I., McDonald, I., Pilachowski, C. A., et al. 2015, AJ, 149, 71
Jones, A., Noll, S., Kausch, W., Szyszka, C., & Kimeswenger, S. 2013, A&A, 560, A91
Karakas, A. I. 2010, MNRAS, 403, 1413
Karakas, A. I., Lattanzio, J. C., & Pols, O. R. 2002, PASA, 19, 515
Kobayashi, C., Karakas, A. I., & Umeda, H. 2011, MNRAS, 414, 3231
Kobayashi, C., Umeda, H., Nomoto, K., Tominaga, N., & Ohkubo, T. 2006, ApJ, 653, 1145
Koleva, M., Prugniel, P., Bouchard, A., & Wu, Y. 2009, A&A, 501, 1269

Koopmans, L. V. E., Bolton, A., Treu, T., et al. 2009, ApJL, 703, L51
Krajnović, D., Cappellari, M., Emsellem, E., McDermid, R. M., & de Zeeuw, P. T. 2005, MNRAS, 357, 1113
Kroupa, P. 2001, MNRAS, 322, 231
Krumholz, M. R. 2014, Physics Reports, 539, 49
Kuntschner, H., Emsellem, E., Bacon, R., et al. 2006, MNRAS, 369, 497
—. 2010, MNRAS, 408, 97
La Barbera, F., Ferreras, I., Vazdekis, A., et al. 2013, MNRAS, 433, 3017
Lauer, T. R., Faber, S. M., Gebhardt, K., et al. 2005, AJ, 129, 2138
Leauthaud, A., Tinker, J., Bundy, K., et al. 2012, ApJ, 744, 159
Lecureur, A., Hill, V., Zoccali, M., et al. 2007, A&A, 465, 799
Marchesini, D., van Dokkum, P. G., Förster Schreiber, N. M., et al. 2009, ApJ, 701, 1765
Martín-Navarro, I., Barbera, F. L., Vazdekis, A., Falcón-Barroso, J., & Ferreras, I. 2015a, MNRAS, 447, 1033
Martín-Navarro, I., La Barbera, F., Vazdekis, A., et al. 2015b, ArXiv e-prints
Martín-Navarro, I., Vazdekis, A., La Barbera, F., et al. 2015c, ArXiv e-prints
McDermid, R. M., Cappellari, M., Alatalo, K., et al. 2014, ApJL, 792, L37
McDermid, R. M., Alatalo, K., Blitz, L., et al. 2015, MNRAS, 448, 3484
McLean, I. S., McGovern, M. R., Burgasser, A. J., et al. 2003, ApJ, 596, 561
Meynet, G., & Maeder, A. 2002a, A&A, 381, L25
—. 2002b, A&A, 390, 561
Mowlavi, N. 1999, A&A, 350, 73
Naab, T., Johansson, P. H., & Ostriker, J. P. 2009, ApJL, 699, L178
Naab, T., Oser, L., Emsellem, E., et al. 2014, MNRAS, 444, 3357
Noeske, K. G., Weiner, B. J., Faber, S. M., et al. 2007, ApJL, 660, L43
Noll, S., Kausch, W., Barden, M., et al. 2012, A&A, 543, A92
Noll, S., Kausch, W., Kimeswenger, S., et al. 2014, A&A, 567, A25
Norris, J., & Pilachowski, C. A. 1985, ApJ, 299, 295
Oke, J. B., Cohen, J. G., Carr, M., et al. 1995, PASP, 107, 375
Oser, L., Naab, T., Ostriker, J. P., & Johansson, P. H. 2012, ApJ, 744, 63
Paltoglou, G., & Norris, J. E. 1989, ApJ, 336, 185
Pastorello, N., Forbes, D. A., Foster, C., et al. 2014, MNRAS, 442, 1003
Patel, S. G., van Dokkum, P. G., Franx, M., et al. 2013, ApJ, 766, 15
Peacock, M. B., Zepf, S. E., Maccarone, T. J., et al. 2014, ApJ, 784, 162
Podorvanyuk, N. Y., Chilingarian, I. V., & Katkov, I. Y. 2013, MNRAS, 432, 2632
Posacki, S., Cappellari, M., Treu, T., Pellegrini, S., & Ciotti, L. 2015, MNRAS, 446, 493
Puzia, T. H., Saglia, R. P., Kissler-Patig, M., et al. 2002, A&A, 395, 45
Ramírez, S. V., & Cohen, J. G. 2002, AJ, 123, 3277
Renzini, A. 2008, MNRAS, 391, 354
Renzini, A., & Voli, M. 1981, A&A, 94, 175
Rockosi, C., Stover, R., Kibrick, R., et al. 2010, in Society of Photo-Optical Instrumentation Engineers (SPIE) Conference Series, Vol. 7735, Society of Photo-Optical Instrumentation Engineers (SPIE) Conference Series, 0
Roediger, J. C., Courteau, S., Graves, G., & Schiavon, R. P. 2014, ApJS, 210, 10
Salmon, B., Papovich, C., Finkelstein, S. L., et al. 2015, ApJ, 799, 183
Salpeter, E. E. 1955, ApJ, 121, 161
Sánchez, S. F., Kennicutt, R. C., Gil de Paz, A., et al. 2012, A&A, 538, A8
Sánchez-Blázquez, P., Peletier, R. F., Jiménez-Vicente, J., et al. 2006, MNRAS, 371, 703
Sarzi, M., Falcón-Barroso, J., Davies, R. L., et al. 2006, MNRAS, 366, 1151
Schiavon, R. P. 2007, ApJS, 171, 146
Scott, N., Cappellari, M., Davies, R. L., et al. 2009, MNRAS, 398, 1835
Serven, J., & Worthey, G. 2010, AJ, 140, 152
Serven, J., Worthey, G., & Briley, M. M. 2005, ApJ, 627, 754
Shankar, F., Marulli, F., Bernardi, M., et al. 2013, MNRAS, 428, 109
Smit, R., Bouwens, R. J., Franx, M., et al. 2012, ApJ, 756, 14
Smith, R. J., & Lucey, J. R. 2013a, MNRAS, 434, 1964
—. 2013b, MNRAS, 434, 1964
Smith, R. J., Lucey, J. R., & Carter, D. 2012, MNRAS, 426, 2994
Smith, R. J., Lucey, J. R., & Conroy, C. 2015, MNRAS, 449, 3441
Spiniello, C., Trager, S., Koopmans, L. V. E., & Conroy, C. 2014, MNRAS, 438, 1483
Spiniello, C., Trager, S. C., & Koopmans, L. V. E. 2015, ApJ, 803, 87
Spiniello, C., Trager, S. C., Koopmans, L. V. E., & Chen, Y. P. 2012, ApJL, 753, L32
Strader, J., Seth, A. C., Forbes, D. A., et al. 2013, ApJL, 775, L6
Strom, S. E., Strom, K. M., Goad, J. W., Vrba, F. J., & Rice, W. 1976, ApJ, 204, 684
Tamura, N., Kobayashi, C., Arimoto, N., Kodama, T., & Ohta, K. 2000, AJ, 119, 2134
Tang, B., Worthey, G., & Davis, A. B. 2014, MNRAS, 445, 1538
Thomas, D., Greggio, L., & Bender, R. 1999, MNRAS, 302, 537
Thomas, D., Maraston, C., Bender, R., & Mendes de Oliveira, C. 2005, ApJ, 621, 673
Trager, S. C., Faber, S. M., & Dressler, A. 2008, MNRAS, 386, 715
Trager, S. C., Faber, S. M., Worthey, G., & González, J. J. 2000a, AJ, 119, 1645
—. 2000b, AJ, 120, 165
Trager, S. C., Worthey, G., Faber, S. M., Burstein, D., & González, J. J. 1998, ApJS, 116, 1
Treu, T., Auger, M. W., Koopmans, L. V. E., et al. 2010, ApJ, 709, 1195
Trujillo, I., Förster Schreiber, N. M., Rudnick, G., et al. 2006, ApJ, 650, 18
van der Wel, A., Franx, M., van Dokkum, P. G., et al. 2014, ApJ, 788, 28
van Dokkum, P. G., & Conroy, C. 2010, Nature, 468, 940
—. 2012, ApJ, 760, 70
van Dokkum, P. G., Whitaker, K. E., Brammer, G., et al. 2010, ApJ, 709, 1018
Vazdekis, A., Ricciardelli, E., Cenarro, A. J., et al. 2012, MNRAS, 424, 157
Ventura, P., & D'Antona, F. 2008a, A&A, 479, 805
—. 2008b, MNRAS, 385, 2034
—. 2009, A&A, 499, 835
Vulcani, B., Bundy, K., Lackner, C., et al. 2014, ApJ, 797, 62
Weijmans, A.-M., Cappellari, M., Bacon, R., et al. 2009, MNRAS, 398, 561
Wilkinson, D. M., Maraston, C., Thomas, D., et al. 2015, MNRAS, 449, 328
Woosley, S. E., & Weaver, T. A. 1995, ApJS, 101, 181
Worthey, G., Faber, S. M., Gonzalez, J. J., & Burstein, D. 1994, ApJS, 94, 687
Wuyts, S., Förster Schreiber, N. M., van der Wel, A., et al. 2011, ApJ, 742, 96
Zahid, H. J., Dima, G. I., Kudritzki, R.-P., et al. 2014, ApJ, 791, 130